Apatite LA-ICP-MS U-Pb and fission-track geochronology of the Caño Viejita gabbro in E-Colombia: Evidence for Grenvillian intraplate rifting and Jurassic exhumation in the NW Amazonian Craton.

Amed Bonilla, Jose Franco, Thomas Cramer, Marc Poujol, Nathan Cogné, Simon Nachtergaele, Johan de Grave

Apatite LA-ICP-MS U-Pb and fission-track geochronology of the Caño Viejita gabbro in E-Colombia: Evidence for Grenvillian intraplate rifting and Jurassic exhumation in the NW Amazonian Craton.

Amed Bonilla[a], Jose A. Franco[a], Thomas Cramer[a], Marc Poujol[b], Nathan Cogné[b], Simon Nachtergaele[c] & Johan De Grave[c].

a. Geoscience Department, National University of Colombia, Bogotá, Colombia. abonillape@unal.edu.co, Calle 23c # 69f-65 Int 27 apto 502.
b. Universitè de Rennes, CNRS, Géosciences Rennes - UMR 6118, F-35000 Rennes, France
c. Department of Geology, Ghent University, Krijgslaan 281.S8, WE13, 9000 Ghent, Belgium

ABSTRACT

The 1.80-1.76 Ga crystalline basement in Colombia as part of the W-Amazonian Craton is composed mainly of gneisses, granitoids and migmatites, affected later by several compressive and extensional events resulting for example in A-type granites, but also mafic intrusions and dikes. Here we present, after a revision of main geological features, research results obtained on the NW-SE trending ilmenite-apatite-rich Caño Viejita gabbro in the SW-Vichada department some 500 km east of Bogota. Petrographic and geochemical data hint to a metaluminous continental alkaline gabbro enriched in K, Ti and P, possibly due to continental crust reworking or magma mixing, as also confirmed by trace elements characteristics in the apatites like HREE enrichment $(Ce/Yb)_{cn}$ 12-13, negative Eu-anomaly, and Y, Th, Sr, Mn ratios. LA-ICP-MS U-Pb apatite geochronology suggests an early Neoproterozoic emplacement age between 975±9 and 1002±21 Ma related with rifting triggered by the Amazonia-Baltica-Laurentia collision during the Rodinia Supercontinent assembly and associated Grenvillian events. These events also caused mafic intrusions in other parts of the craton. Apatite fission track thermochronometry and thermal history

modelling on one sample suggest the onset of the final exhumation stage during Jurassic (~180 Ma), which brought the rocks slowly to their current outcrop position.

Keywords: U-Pb apatite chronology, apatite fission-track thermochronology, olivine gabbro, Amazonian Craton, Neoproterozoic, Grenvillian.

1. Introduction

The Amazonian Craton is one of the largest Precambrian continental nuclei in the world comprising huge parts of NW-South America, mainly in Brazil, but also in Venezuela, Guyana, Suriname, French Guyana and NE-Colombia. It formed during the Paleo-Mesoproterozoic due to several accretion events, was affected by extensional and crust consuming episodes, which all resulted in complex geochronological provinces (**Error! Reference source not found.**). These provinces have been (re)defined and refined over the last years and the exact positions of their boundaries is still a matter of debate (Cordani et al., 2009, 1979; Kroonenberg, 2019; Santos et al., 2000; Tassinari and Macambira, 1999; Teixeira et al., 1989). The NW Amazonian Craton that outcrops in Eastern Colombia yields ages between ~1.86-1.70 Ga and is defined as part of the Mitú Migmatitic Complex (Galvis et al., 1979; Rodríguez et al., 2011) or better the Mitú Complex (Bonilla et al., 2019; López et al., 2007). This Mitú Complex is itself a portion of the 1.86-1.55 Ga Rio Negro-Juruena Geochronological Province (Tassinari et al., 1996; Tassinari and Macambira, 1999). Older (~1.98 Ga) metavolcanic rocks of the Atabapo-Río Negro Gneiss may testify remains of the Trans-Amazonian basement (Kroonenberg, 2019) and not of the Mitú Complex accretion. This complex was affected by several magmatic and tectonic episodes during the Mesoproterozoic (1.6-1.0 Ga), among them (in Colombia 1.40-1.34 Ga) intraplate A-type

56 granite emplacements like the Parguaza and Matraca rapakivi granites (Bonilla et al., 2013;
57 Bonilla et al., 2016; Gaudette et al., 1978) and the Nickerie-K'Mudku thermal event 1.3-1.0
58 Ga ago deduced from far-reaching K/Ar and Rb/Sr ages resetting.
59
60 The youngest of the geochronological Amazonian Craton provinces identified hitherto is the
61 1.25-1.0 Ga old Sunsás Province (**Error! Reference source not found.**), a late
62 Mesoproterozoic collisional metamorphic belt in the southwestern margin of the Amazonian
63 Craton which constitutes an important paleogeographic link between the late Meso- and the
64 early Neoproterozoic, when Amazonia, Baltica and Laurentia became part of the Rodinia
65 supercontinent first proposed by Hoffman (1991) and confirmed by further studies (Cardona
66 et al., 2010; Cordani et al., 2010, 2009; Dewanckele et al., 2014). There is no reason why
67 younger accretionary belts, like the Rondonia-San Ignacio (1.55–1.3 Ma) and the Sunsás
68 (1.25–0.99 Ga) orogenic belts in the southern block, should not extend below the Amazon
69 Basin until the North Andean foreland. Covered by thick Cenozoic sediments (Cordani et al.,
70 2009; Santos et al., 2000; Tassinari and Macambira, 1999, 2004) and with dense tropical
71 forest and soils, their identification is difficult. However, several Grenvillian-age basement
72 inliers were identified in the northern Andes of Colombia (Figure 2), Ecuador and Peru (see
73 e.g. Restrepo-Pace and Cediel, 2010), although their lithostratigraphic and tectonic history
74 seem to differ somehow from that of the Sunsás belt.

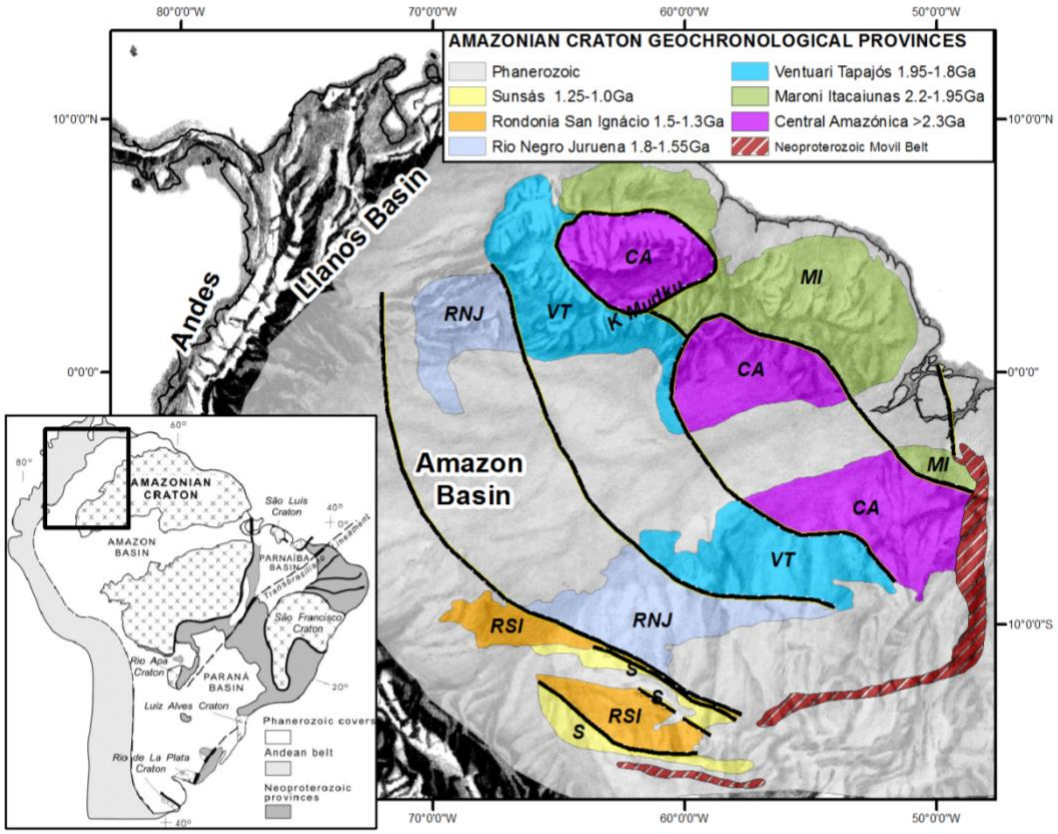

Figure 1 The Amazonian Craton in South America and Geochronological Provinces after Tassinari and Macambira (1999). CA: Central Amazonica, MI: Maroni-Itacaiunas, VT: Ventuari-Tapajos, RNJ: Rio Negro-Juruena, RSI: Rondonia-San Ignacio, S: Sunsás. The extended Phanerozoic sediments W of the Andes as those filling the Llanos Basin cover large parts of the Pre-Cenozoic rocks, and only small portions of Precambrian units like the Sunsás geochronological province the area of the (S) were identified hitherto in Colombia.

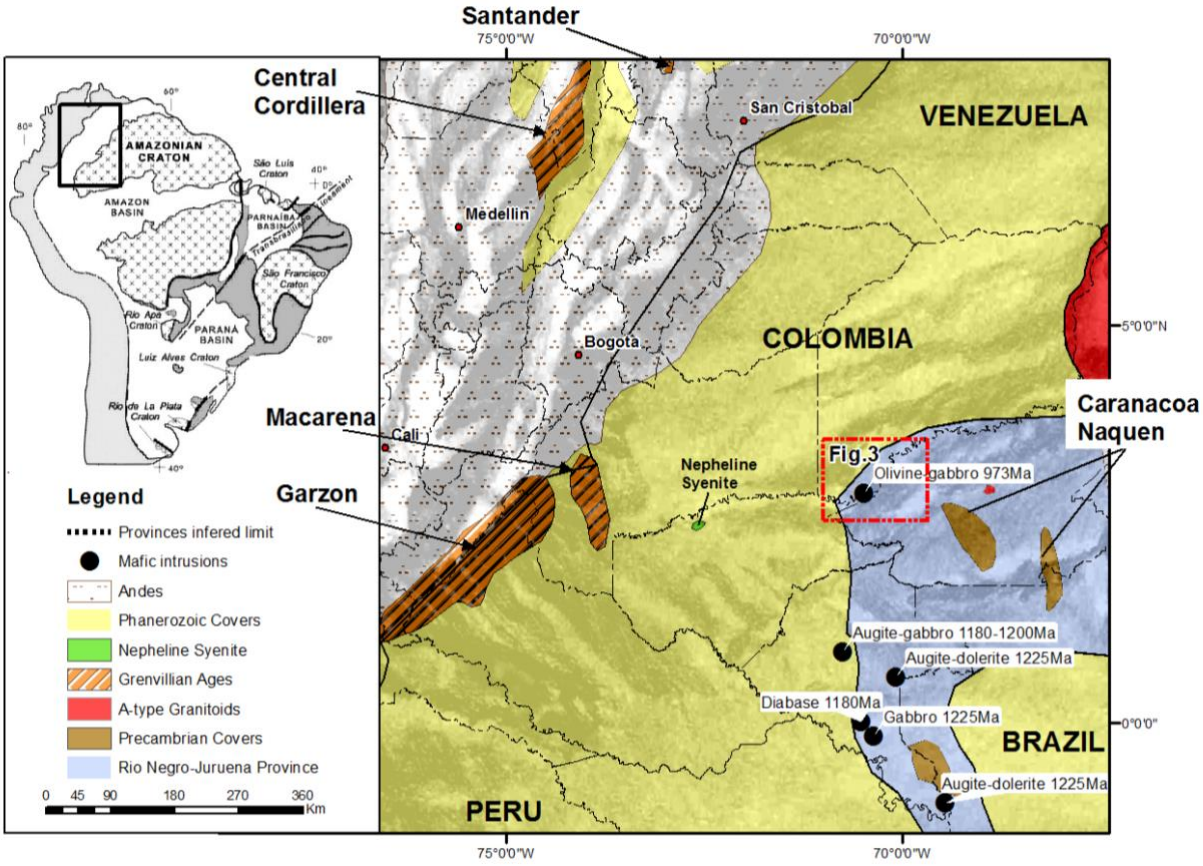

Figure 2 Location of the study area (red rectangle within the blue-marked Rio Negro-Juruena Province) in the Colombian part of the NW Amazonian Craton. Also shown are A-type granitoids to the East (Parguaza and Matraca rapakivi granites), Grenvillian-age remnants to the West near and within the Andes, the Ecarian to Cambrian Nepheline Syenite of San Jose de Guaviare, Precambrian (Caranacoa and Naquén) to Phanerozoic covers and ages of some mafic rock outcrops (Table 1). Modified after Cordani et al., 2010; Tassinari and Macambira, 1999; Ibañez et al., 2011, 2016; Bonilla et al., 2016.

Consequently, this belt could represent a separate composite orogeny (Cardona et al., 2010; Ibañez, 2010). Based on drill core sample analyses, Ibañez (2010) suggested the existence of a younger orogenic belt in Colombia called the “Putumayo Orogen” assumed to be coeval with the Sunsás belt. Both have a distinctly different posterior geological evolution, resulting, amongst others, in different structure and fabric. The Putumayo Orogen is marked by two evolutionary stages in a Rodinian context: i.e. an early tectonometamorphic event (1.05 Ga), followed by anatectic melting (1.01 Ga) resulting from an inferred arc-continent collision

98 followed by a final continent-continent collision and associated granulite–facies
99 metamorphism (~0.99 Ga) (Ibañez et al., 2015; Ibañez, 2010). Relics of both events are
100 found sporadically along the Colombian Andes as basement inliers (Figure 2) with U-Pb
101 zircon ages of ~1.1- 0.99 Ga (Cardona et al., 2010; Ibañez et al., 2015; Ibañez, 2010;
102 Restrepo-Pace, 1995) possibly as product of a continent-continent collision (Amazonia-
103 Baltica in this case) during the aggregation of the Mesoproterozoic supercontinent Rodinia,
104 as first proposed by Hoffman (1991). Rivers (1997) suggested three orogenic pulses in the
105 Canadian Grenville province, the Elzevirian (starting ~1.35 Ga), Ottawan (~1.15 Ga) and
106 Rigolet (~1.0 Ga). Only the last episode (Rigolet) has affected the entire magmatic-tectonic
107 Grenville-province where indeed the Sunsás-belt acted as the Amazonia-Baltica counterpart
108 of the Grenville belt on the Laurentia side during the collision that culminated in the final
109 amalgamation of the Rodinia supercontinent.
110
111 Several intraplate rifting events have been recognized in the Amazonian Craton as responses
112 to the collisions at its borders (Cordani et al., 2010; Santos et al., 2008; Teixeira et al., 2010).
113 In the whole Rio Negro-Juruena Province, anorogenic granite intrusions with ages between
114 1.6-0.97 Ga are reported (Bettencourt et al., 1999; Bonilla et al., 2013; Dall'Agnol et al., 1999;
115 Gaudette et al., 1978; Bonilla et al., 2016), whereas the less common mafic to ultramafic
116 intrusive rocks yield Rb-Sr and K-Ar whole-rock isochron ages between 1.20-0.94 Ga (Priem
117 et al., 1982; Tassinari et al., 1996; Teixeira and Tassinari, 1976). In the SW-Amazonian
118 Craton some mafic rocks associated with a rift system as response to the Sunsás orogeny
119 form part of a well-defined convergent active margin (Cordani et al., 2010; Santos et al.,
120 2008; Teixeira et al., 2010). This indicates that while the western side of the Amazonian
121 Craton (Amazonia) was colliding against Baltica and Laurentia to build Rodinia, expressing

itself in the Grenvillian-Sunsás orogeny, rifting had already initiated further inland during the Late Mesoproterozoic-Early Neoproterozoic (Cordani et al., 2010; Teixeira et al., 2010).

In this work, we show further evidence of Grenvillian-age mafic rift or intraplate magmatism in the NW Amazonian Craton in Colombia based on petrographic, geochemical and U-Pb apatite LA-ICP-MS analysis of the NW-SE trending ilmenite-apatite-rich Caño Viejita gabbro in the SW-Vichada department some 500 km east of Bogota. Apatite fission-track thermochronometry suggests furthermore a continuous exhumation and denudation process of these rocks since the Jurassic until their current outcrop position.

2. Geological and tectonic setting

The Colombian part of the Amazonian Craton, which represents less than 10% of this Precambrian nucleus in South America, outcrops in Vichada, Guainía, Vaupés, Caquetá and Guaviare departments (**Error! Reference source not found.** and Figure 2) but is largely covered by thick sedimentary sequences in the Amazonas and Llanos basins as weathering and erosion products of its complex history.

2.1 Eastern Colombian basement (1800-1500Ma)

Since the 1960's, important progress has been made in the understanding of the geological evolution of this region which was initially simply named the Basement Group (Gansser, 1954). Especially different national remote sensing programs (e.g. Departamento Nacional da Producäo Mineral, 1976; Huguett, 1977; Kroonenberg and de Roever, 2010; PRORADAM, 1979; Putzer, 1984) and dedicated field work produced a wealth of new data. These studies have led in the 70$_{th}$ to the recognition of the Mitú Migmatitic Complex (Galvis et al., 1979; Rodríguez et al., 2011), later called the Mitú Complex (Bonilla et al., 2019; López et al., 2007)

148 as part of the 1.80-1.55 Ga Rio Negro-Juruena Geochronological Province (Figure 2) in
149 Colombia (Tassinari et al., 1996; Tassinari and Macambira, 1999). Large parts of the Mitú
150 Complex (Figure 3) are composed of monzogranites with calc-alkaline characteristics, and
151 meta- to peraluminous affinity with an U-Pb LA-MC-ICPMS age for the Mitú granite of 1574 ±
152 10 Ma (Ibáñez-Mejía et al. 2011), as well as of other granites: Among the clearly
153 metamorphic rocks prevail quartzo-feldspathic gneisses with zircon U-Pb ages between
154 1800-1760 Ma (Bonilla et al., 2019; Cordani et al., 2016; Kroonenberg, 2019; López et al.,
155 2007). Medium grade amphibolite facies metamorphic rocks within a series of essentially
156 juvenile magmatic arcs in the Rio Negro Juruena province are interpreted as subduction-
157 related by several workers (Cordani et al., 2016; Tassinari and Macambira, 1999).

158 Younger granitoids in its SE-part (especially Guainia Department) exhibit variable
159 compositions, porphyritic textures and may contain ovoid feldspar phenocrysts that
160 crystallized some 1750 Ma ago during the Statherian (Bonilla et al., 2019).

161 On this Statherian basement, a metasedimentary sequence, associated with the Tunui Group
162 in Brazil (Almeida et al., 2004; Santos et al., 2003) was deposited about 1720 - 1600 Ma ago
163 (Bonilla et al., 2019) and extends to the north into the Naquen and Caranacoa mountains
164 (Figure 2). This Precambrian cover in the south of Guainia Department contains an upper
165 quartzite facies, partly tourmalinized, locally influenced by metasomatism which may be
166 responsible for gold deposits in this area and associated with a two-mica granite intrusion
167 some 1600-1550 Ma ago (Bonilla et al., 2019). The latter is probably part of the Rio Içana
168 Intrusive Suite described in Brazil (Almeida et al., 2004; Almeida and Larizzatti, 1996;
169 Carneiro et al., 2017a, 2017b; Veras, 2012), and evolved by partial melting of cratonic
170 protoliths (Almeida et al., 1997). In a similar way, other ~1600 – 1500 Ma old granites have

been described along the whole Colombian eastern territory (Cordani et al., 2016; Ibañez, 2010; Priem et al., 1982; Rodriguez et al., 2011).

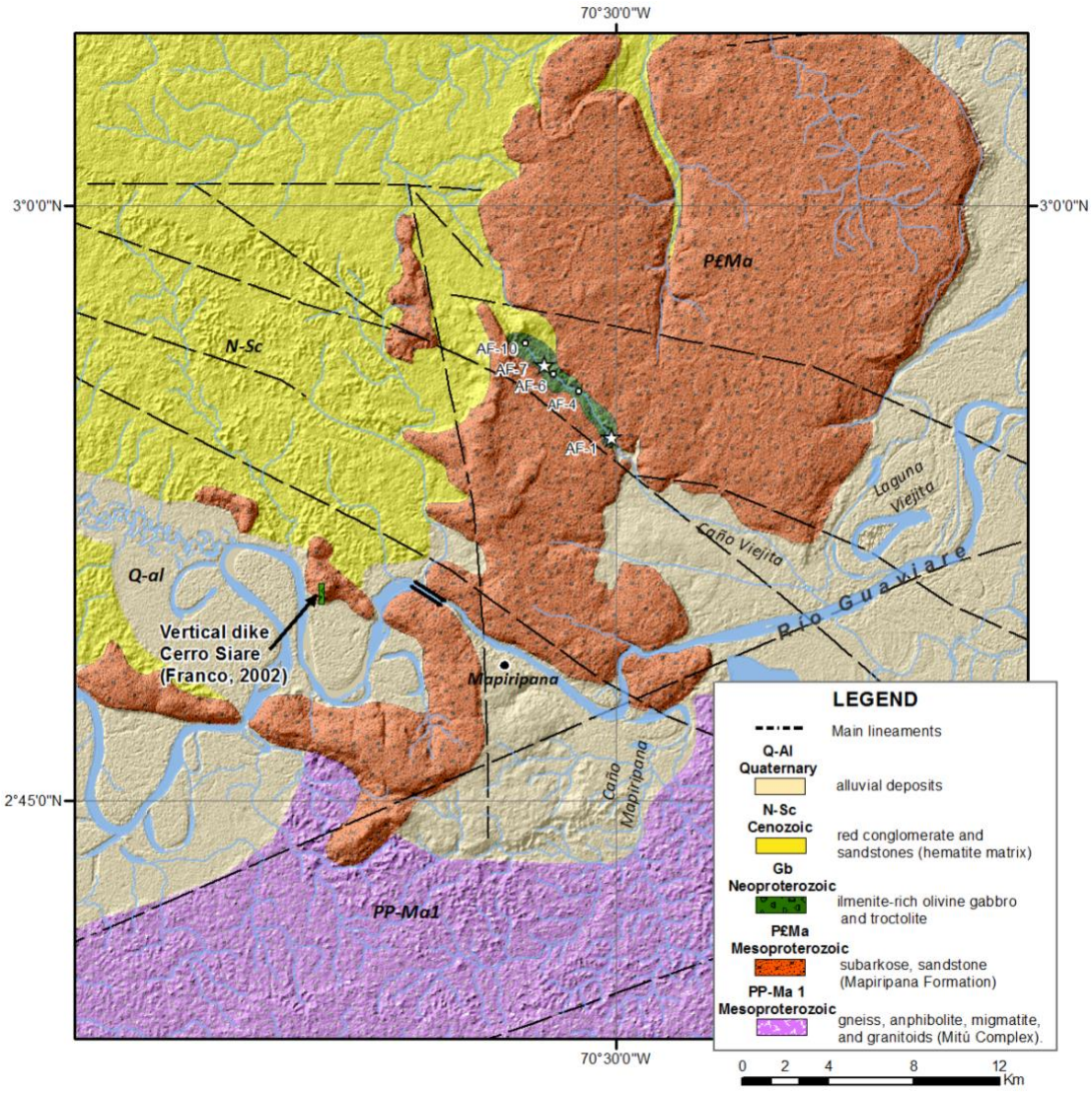

Figure 3 Geological map of the study area (red rectangle in **Figure 2**) with sampling points AF in the NW-trending gabbro surrounded by possibly Mesoproterozoic sedimentary rocks (modified from Franco et al., 2014; Franco et al., 2002; Gómez Tapias et al., 2015). Observe also the vertical gabbro dike at Cerro Siare crosscutting the sediments described by Franco et al. (2002).

2.2 Anorogenic magmatism (1500-1000 Ma)

Several rapakivi intrusive suites in the Brazilian SW-Amazonian Craton (e.g. Santo Antonio,

183 Teotonio, Alto Candeias) represent extensional anorogenic magmatism associated with the
184 terminal stages of the Rondonian–San Ignacio Orogeny ~ 1.50 to 1.30 Ga (Bettencourt et al.,
185 1999). Also in the NW-part of the Rio Negro-Juruena Province in Colombia, evidence of rift or
186 intraplate magmatism exists, including ~1.40 to 1.34 Ga rapakivi granite intrusions like the
187 Parguaza and Matraca rapakivi granites (Bonilla et al., 2013; Bonilla et al., 2016; Gaudette et
188 al., 1978). Later, the regional tectono-thermal "Nickerie-K'Mudku" event affected the area and
189 temperatures above 300°C resetted (partially) the Rb-Sr and K-Ar systems, leaving 1300 –
190 1000 Ma cooling ages (Cordani et al., 2016; Galvis et al., 1979; Priem et al., 1982).
191
192 Younger <1.0 Ga intra-plate A-type granites in the SW-Amazonian Craton (Teixeira et al.,
193 2010) produced by extensional tectonics and rifting resulting from collisional events ~1.25 to
194 1.0 Ga (Teixeira et al., 2010) are until now unknown in the NW Amazonian Craton.
195
196 Less prominent than the felsic intrusions, but locally important, mafic intrusions and dikes
197 occur in the Amazonian Craton, as for example on its western margin, where they are mainly
198 of Grenvillian age (**Error! Reference source not found.**). Unfortunately, the current tropical
199 climate and associated strong weathering reduce the number of outcrops for this rare rock
200 types even more. Where they are visible, they cross-cut the basement or the overlying meta-
201 sedimentary sequences along pre-existing major NE–SW or NW–SE trends forming dikes
202 dated by Rb/Sr-whole-rock analyses between 1225-1100 Ma (Priem et al., 1982). Teixeira et
203 al. (2010) describe mafic dikes, sills and graben basins as product of post-tectonic to
204 anorogenic stages in the SW Amazonian Craton that took place after ca. 1 Ga.

205 **Table 1** Mafic rocks of Grenvillian age reported in the NW and SW Amazonian Craton
206 margin**.**

Location and Rock type	Age (Ma)	Method and Reference
NW Amazonian Craton		
Papuri River: Augite-dolerite	1225	Rb/Sr whole rock, Priem (1982) Figure 2

Serra Traira, NW Brazil: Dolerite dikes	940–980	K–Ar, Tassinari (1996)
North of Manaus, Amazonas: Gabbro intrusion	1100	K–Ar, Teixeira (1978); Tassinari (1996)
Pira-Parana River: Diabase dike,	1180	Rb/Sr, whole rock Priem (1982) Figure 2
Augite-gabbro	1200	Rb/Sr whole rock, Priem (1982) Figure 2
Augite-gabbro	1180	Rb/Sr whole rock, Priem (1982) Figure 2
SW Amazonian Craton		
Northern Rondonia State of Brazil: dolerite dikes, gabbros and alkaline intrusions	1050–1200	K–Ar + Rb–Sr Teixeira (1978), Tassinari (1996)
Southern Rondonia State of Brazil: dolerite dike swarms	1000–1100	K–Ar Teixeira (1978), Tassinari (1996)

207

208 **2.3 Post Mesoproterozoic events**

209

210 The youngest known intracratonic magmatic episode in the NW Amazonian Craton is a rift-
211 related alkaline subsiliceous event (Nepheline Syenite of San José del Guaviare) with
212 Neoproterozoic-Ediacaran to Cambrian ages (U-Pb zircon emplacement ages) of ~578 Ma
213 (Mejia et al., 2012) and biotite K-Ar and Rb-Sr cooling ages of 445 – 495 Ma (Pinson et al.,
214 1962). Recent own LA-ICP-MS U-Pb zircon ages of ~ 609 Ma (Franco et al., 2018; Muñoz
215 Rocha et al., 2019) near Jordan to the SE of the intrusion, suggest a long emplacement and
216 cooling history for this large body that is probably associated with the Pan-African - Braziliano
217 orogeny. Further west, no intracratonic intrusions are reported.

218

219 Since early Phanerozoic, predominant uplift and erosion of the NW Amazonian Craton are
220 evidenced by large stratigraphic hiatus, interrupted by several transgressions and marine
221 depositional regimes during the Paleozoic (e.g. Silurian (?) sandstone Araracuara Formation,
222 NW-trending Güejar- Apaporis Graben filled with marine platform and continental sediments).

The Colombian Cretaceous Transgression, which extended at least to the modern Eastern Cordillera at the western Amazonian Craton boundary, was the most prominent expression of a Pre-Andean extension. It encompassed various back-arc zones with recognizable syn- and post-rift phases of basin evolution (Horton, 2018) as result of an intensification of the Nazca plate subduction below the incipient South American continent in its modern form. The related rapid uplift, erosion and exhumation of the Amazonian Craton caused widespread Mesozoic stratigraphic gaps all over the craton's cover and a high flux of recycled Precambrian sourced sediments filling the Andes or Llanos Basin (Cardona et al., 2011) mainly in east – west directed fluvial systems.

The Cenozoic Andean history shows a less pervasive extension in the midst of the Andean orogeny and affected specific fore-arc lowlands, elevated hinterland regions, and isolated retro-arc settings (Horton, 2018). Also, since the Paleogene, the Andean orogeny changed the fluvial systems in the Colombian Amazonian Craton with its continental sedimentary cover now directing the rivers eastwards to the Orinoco Basin or to the Amazonian Basin.

3. Methods

3.1 Field work

During a 2010 exploration survey in a black sands mining concession area (#18557 mining cadaster code), we found that the main ore minerals there were alluvial ilmenite concentrates which obviously resulted from the weathering of a mafic intrusive body in the SW of the Vichada Department. The source gabbro outcrops along a 6 km small creek called "Caño Viejita", a tributary of the Guaviare River (Figure 3). The elongated gabbro trends N40W with unclear extension, as to the north it is limited by a river and a ~50 m thick sedimentary

sequence that outcrops as “Tepui” with <10° N dip, and is fringed by vertical cliffs (Figure 4A). The tropical climate produced abundant spheroidal weathering forms (Figure 4B) and yellowish weathering rims on the rock samples; it is not clear until which point abundant secondary minerals like chlorite and serpentine are product of this weathering or syn- to postmagmatic fluids. More field data are presented in the result and discussion chapters. High ilmenite content visible in the fresh rock (Figure 4C) results in placer deposits as weathering product of the gabbro. For this area, where presumably the ilmenites were mined as titanium ore, also a mining license had been emitted years ago by the Colombian authorities for wolframite, coltan and other alluvial “black sands” which served mainly for “laundering” of wolframite and coltan illegally mined from other deposits in E-Colombia like Cerro Tigre in the Guainía department. This illustration of the complex interaction between geology, mining, lack of knowledge and both social, political and environmental issues portrays the challenges of geologists in Colombia, but thanks to further exploration efforts of the title owner in this case facilitated field recognition and sampling of black sands, soils and fresh rocks which were brought to Bogotá for further analyses.

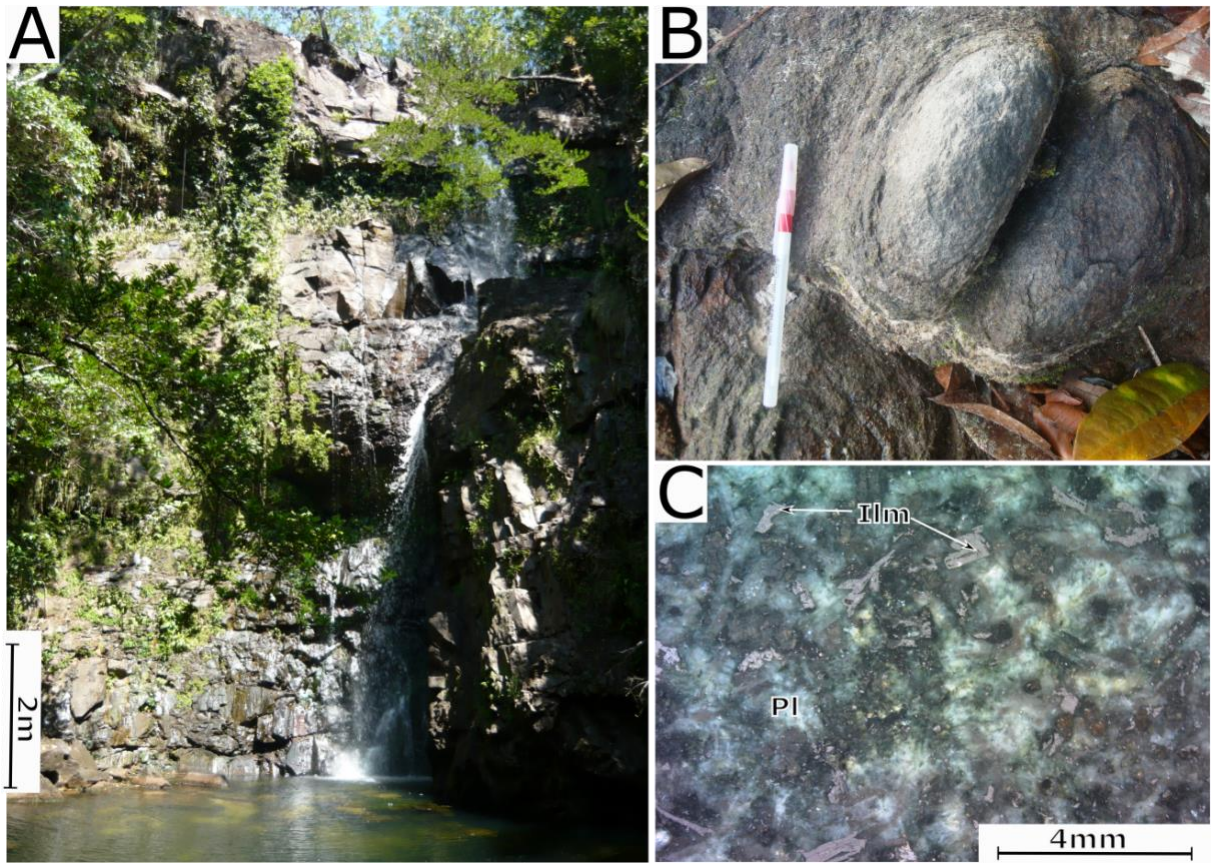

Figure 4 Some geological features in the study area: A) sub-horizontal layers of the Mesoproterozoic sedimentary sequence with characteristic waterfall of the Viejita creek with ilmenite concentrates; B) spheroidal forms resulting from tropical weathering of the gabbro; C) Binocular image (10x) of ilmenite crystals in plagioclase and pyroxene, within an undeformed gabbro texture.

3.2 Petrography and whole rock geochemistry

Seven thin sections from different parts of the gabbro were analyzed under a Zeiss Axio Scope A1 petrographic microscope. Whole rock geochemistry by means of XRF was carried out on 3 samples (Af-1, Af-7 and Af-4, the first two were also used for U-Pb apatite geochronology, and sample Af-4 was measured one year later for quality control). The samples were pulverized and mixed with Merck spectromelt wax at sample/wax ratio of 10/1 and measured with a Phillips MagixPro PW - 2440 X-ray fluorescence spectrometer (4 kW, Rh-tube, reported detection limit 20 ppm for heavy elements) at the National University of

Colombia. For interpretation and diagrams, mainly the GCDkit5.0 software (Janousek et al., 2008) was used. By means of LA-ICP-MS, REE of extracted apatites were measured, which will be discussed later.

3.3 Apatite U-Pb LA-ICP-MS geochronology

Mineral separation procedures on two crushed gabbro samples (Af-1 and Af-7) at Universidade Federal do Rio Grande do Sul (Brazil) yielded too low datable zircon or baddeleyite contents in the concentrates, but sufficient apatite crystals of good quality after applying conventional mineral separation techniques. From the non-magnetic heavy fraction, apatite grains were carefully handpicked under a binocular microscope, embedded in epoxy resin and afterwards grounded and polished with a 6, 3 and 1µm diamond suspension successively.

In the first sample (Af-1), apatite cathodoluminescence (CL) images were acquired using a Reliotron CL system equipped with a digital color camera at Géosciences University Rennes, where also LA-ICP-MS U-Pb geochronology was conducted using an ESI NWR193UC Excimer laser coupled to a quadripole Agilent 7700x ICP-MS equipped with a dual pumping system to enhance sensitivity (Paquette et al., 2014). During the analyses, we used an ablation spot diameter of 50 µm, a repetition rate of 5 Hz and a fluence of 6.5 J/cm². Data were corrected for U-Pb and Th-Pb fractionation and for the mass bias by standard bracketing with repeated measurements of the Madagascar apatite standard (Cochrane et al., 2014). The apatite standards McClure (523.51 ± 2.09 Ma (Schoene and Bowring, 2006)) and Durango (31.44 ± 0.18Ma (McDowell et al., 2005)) which were used during the measurements to monitor precision and accuracy of the analyses, yielded ages of 520 ± 9

(McClure, N = 3, MSWD = 0.47) and 32.3 ± 0.8 Ma (Durango, N = 5, MSWD = 0.76). For instrumental conditions and protocols used in this study see Pochon et al. (2016) and Table 3.

A different protocol was necessary for the second apatite samples (Af-7), on which also fission track analysis were performed, as well as additional trace elements determinations (mainly Cl, Ca, REE) using the same shots as for the U-Pb ages. The same LA-ICP-MS facility as described above was used, but with a spot size of 30 µm, a repetition rate of 7 Hz and a fluence of 6 J/cm$_2$. The full instrumental conditions and U-Pb dating protocol are reported in Table 3, too. In the same way as the first sample, data were corrected for U-Pb and Th-Pb fractionation and for the mass bias by standard bracketing with repeated measurements of the Madagascar apatite standard (Cochrane et al., 2014). The same apatite standards as above used as secondary standard yielded a weighted mean ^{207}Pb-corrected age of 528.9 ± 7.0 (McClure, N = 11, MSWD = 0.41) and 31.7 ± 2.2 Ma (Durango, N = 24, MSWD = 0.55).

3.4 Apatite Fission Track Thermochronology and trace elements patterns

The apatite fission track (AFT) method is a low-temperature thermochronological technique based on the spontaneous fission of ^{238}U in the apatite crystal lattice. The fission decay produces lattice damage trails, the fission tracks, which can accumulate over time. At geological timescales, fission tracks in apatite are considered stable at temperatures lower than ~60°C, while they anneal completely at temperatures above ~120°C (Ketcham et al., 1999; Wagner and Van den Haute, 1992). Between these two temperature thresholds, fission tracks (initially ~16µm) in apatite are gradually shortened, defining the Apatite Partial

330 Annealing Zone (APAZ), which depends to some extent on the chemical composition of the
331 apatite crystals (Wagner and Van den Haute, 1992). With a minimum of ~100 measured
332 confined fission track lengths, it is statistically viable to model or reconstruct the low-
333 temperature thermal history of the apatite-bearing rock sample (e.g. Ketcham et al., 1999),
334 but 40 track lengths are considered the absolute minimum (Rahn and Seward, 2000). If
335 significantly less than 100 confined tracks could be measured, only a qualitative (and rather
336 speculative) model can be retrieved, and interpretation of the AFT data and accompanied
337 time-temperature model has to be done with care.
338
339 Fission tracks were counted on 800x magnification with a Nikon Eclipse NI-E microscope
340 system and imaged with a DS-Ri2 camera attached to the microscope system. The
341 determination of the uranium concentration for fission track dating followed the analytical
342 protocol of Cogné et al. (2019). In contrast to the LA-ICP-MS absolute calibration approach of
343 Hasebe et al. (2004), which employs the ^{238}U fission-decay constant, a fission-track
344 registration factor and a calibration factor for etching and observation, Cogné et al. (2019)
345 used a modified zeta calibration approach (cf. Hurford and Green, 1983) for LA-ICP-MS
346 apatite U concentration measurements, building on Donelick et al. (2005). The method
347 assumes that the apatite ^{43}Ca signal intensity during a given LA-ICP-MS session acts as a
348 proxy for the volume of apatite ablated, and hence the apatite $^{238}U/^{43}Ca$ ratio yields relative U
349 concentration measurements. In this study, an extensive primary LA-ICP-MS session was
350 undertaken on Durango apatite crystals (31.44 ± 0.18 Ma (2σ) (McDowell et al., 2005)
351 previously counted for fission tracks to yield a primary LA-ICP-MS zeta factor. The
352 uncertainty on the calibration procedure (including the age uncertainty and the counting
353 statistics related to the number of spontaneous tracks counted in the Durango standard) was
354 propagated through to the final zeta calculation. These same Durango apatite crystals were

355 then analyzed in subsequent LA-ICP-MS (along with apatite unknowns for fission-track
356 dating) to yield a session-specific calibration factor on the primary zeta value. Inter-session
357 drift in both the primary and subsequent LA-ICP-MS sessions was corrected for by monitoring
358 the $^{238}U/^{43}Ca$ ratio of NIST612 standard glass. Depth-related variations in U concentration
359 were accounted for by incorporating a function within the Iolite "Trace elements" data
360 reduction scheme that weights appropriately the $^{238}U/^{43}Ca$ ratio with depth. Chlorine
361 measurements are calibrated with a synthetic "Bamble" apatite (e.g. Chew et al. 2016).
362
363 Data reduction for trace-element data acquired on the same spots was undertaken using the
364 freeware Iolite package of Paton et al. (2011), with the "Trace Elements" data reduction
365 scheme. NIST612 was used as primary reference material. Cl concentration measurements
366 followed the analytical protocol of Chew et al. (2016). The ^{35}Cl background-corrected signals
367 for each apatite analysis were normalized to the internal standard (^{43}Ca) and then sample-
368 standard bracketing was employed using synthetic apatites of known Cl concentration
369 (chlorapatite end member 6.81 wt% Cl, (Klemme et al., 2013)) and Durango fluorapatite (0.37
370 wt% Cl).
371
372 ## 4. Results
373
374 ### 4.1 Petrological and geochemical results
375
376 As the N40W trending gabbro body (Figure 3) is covered to the north by thick sedimentary
377 sequences, its real extent is difficult to assess. The vertical cliffs (Figure 4A) with abundant
378 spheroidal weathering forms (Figure 4B) as well as the high ilmenite content in the fresh rock
379 (Figure 4C) and alluvial "black sands" allow to assume that the body is rather large and
380 affected by active (at least until recently) uplift processes. The continuous supergenic

processes are evidenced in the yellowish weathering rims, secondary chloritization and abundant serpentine, although the contribution of syn- or postmagmatic hydrothermal fluids is not clear, and no signs of metamorphic remobilization are visible, neither macro nor microscopically, nor geochemically.

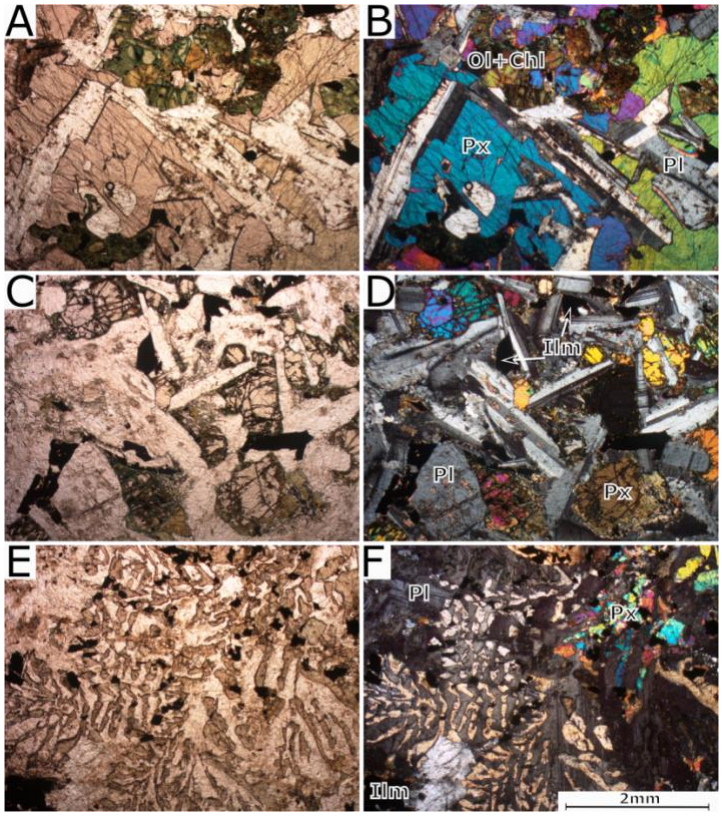

Figure 5 Thin-sections micro-photographs of gabbro samples from Caño Viejita, right side crossed nicols. A-B) olivine-gabbro with interstitial texture showing plagioclase, pyroxene and olivine crystals altered to chlorite; C-D) gabbro with intergranular texture, abundant ilmenite and pyroxene partially altered to chlorite; E-F) gabbro with poikilitic texture where pyroxene laths are enclosed by plagioclase.

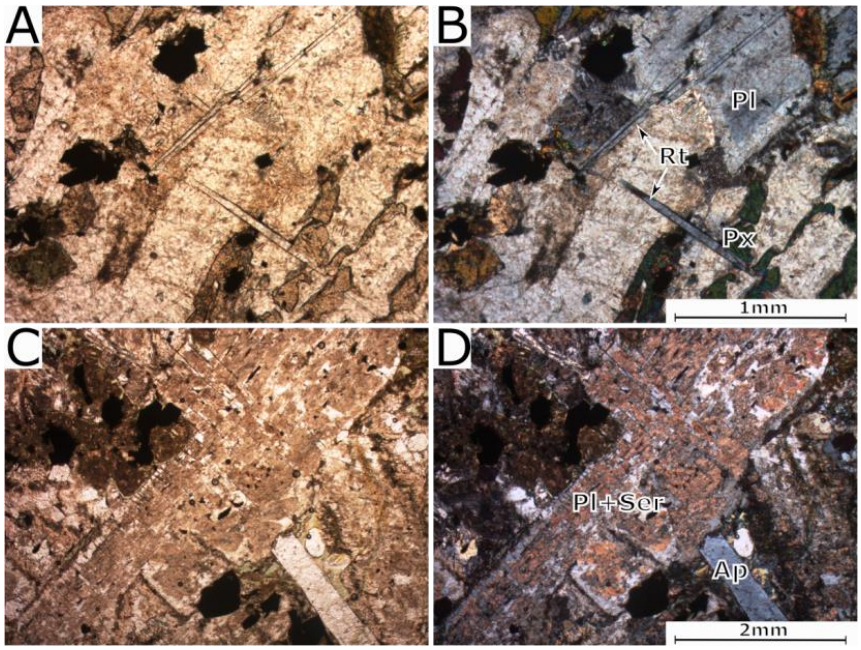

Figure 6 Thin-sections micro-photographs (right XPL) of gabbro samples from Viejita creek, A-B) plagioclase and pyroxene, traversed by acicular rutile crystals; C-D) pronounced replacement of plagioclase by sericite and of olivine by serpentine + chlorite. Observe large apatite crystals and, in both sections, abundant opaque ilmenite grains.

Petrographically, the rock is a gabbro to olivine-gabbro with 58-67% plagioclase (An70), 7-13% clinopyroxene and 4-10% olivine. Abundant accessory minerals (~12%) are ilmenite, rutile, large apatite crystals and pyrite. Neither enough baddeleyite nor zircon were identified for geochronology analyses, thus testifying Si-subsaturation and low Zr-contents (but see note below). Parts of the gabbro exhibit poikilitic texture where large plagioclase phenocrysts enclose skeletal pyroxene crystals (Figure 5E-F) while other portions show interstitial and intergranular textures. Fe-rich olivine (fayalite) is identified due to its slightly higher relief than pyroxene, as well as its fracturing and alteration products like chlorite and serpentine visible in some parts, whereas in the prevailing pyroxenes chlorite alteration dominates. Other alteration minerals are sericite, epidote and iron oxides, as in sample Af-1. Some ~1% biotite in samples Af-6 and Af-7 are associated with ilmenite or pyrite surrounding some olivine crystals. Titanite traces were found in sample Af-1.

XRF data for major and some trace elements are shown in Table 2, together with continental crust gabbro (CCG) values after Le Maitre (1976), cited in Wedepohl (1995) and “normal” gabbro after Nockolds (1954, cited in Perkins, 2014). The geochemistry of the three samples is rather similar, suggesting that they are part of a homogeneous body. The SiO_2 content varies from 46.46 % to 48.15%, which is in the range of a normal gabbros, although with some Si-subsaturation (cf. e.g. https://earthref.org/GERMRD/). High Fe_2O_3 (~13%) reflects itself in fayalite, Fe-pyroxene and, together with high TiO_2 content from 3.12% to 3.43%, in abundant ilmenite and much less rutile in the gabbro. While Al_2O_3 content from 15.55% to 15.83% is typical, K_2O content from 1.86% to 2.04% is rather high for a normal gabbro, thus nearly reaching shoshonite composition, although no K-main minerals were found. On the other hand, CaO from 7.36% to 8.24% and MgO from 4.27% to 4.99% are lower than in oceanic-crust associated gabbro, but CaO is higher than in CCG. High P_2O_5 from 1.54-1.72%

expresses itself in abundant apatite, whereas the low Zr-contents together with Si-subsaturation did virtually not allow zircon crystals to form, although the surely not very precise XRF Zr-values (Table 2) are apparently above the 140 ppm Zr reported for basalts and also a lot of granitic rocks (e.g. Mielke, 1979). Geochemical-petrotectonic discrimination patterns (**Error! Reference source not found.**) such as Na_2O+K_2O vs. SiO_2 (Cox et al., 1979), MgO-FeO_T- Al_2O_3 (Pearce et al., 1977) and TiO_2–K_2O–P_2O_5 (Pearce et al., 1975) locate this intrusive in the field of continental alkaline metaluminous gabbro of Within-Plate characteristics based on the Zr-Y relationship (Pearce and Norry, 1979). Low content together with XRF-detection limits and deficient precision did not allow using other common trace elements like Nb, Ta or most REE for further confident geotectonic interpretations of the gabbro samples.

Table 2 XRF geochemistry of gabbro samples AF-1, AF-4 and AF-7 and of Continental Crust Gabbro (CCG) after Wedepohl (1995, citing Le Maitre (1976)) and "normal" gabbro after Nockolds (1954, cited in Perkins, 2014). Observe the lower SiO_2 and MgO but much higher Na_2O, TiO_2, K_2O and P_2O_5 contents in comparison with CCG and "normal" gabbro, which express in minerals like rutile, and abundant ilmenite and apatite. Only CaO lies between the two gabbro types, possibly reflecting the anorthosite component. Oxides reported in wt.% and trace elements in ppm.

Element	**Af 1**	**Af 4**	**Af 7**	**CCG**	**Gabbro** Nockolds (1954)
SiO_2	48.152	46.46	47.854	50.1	50.78
Al_2O_3	15.833	15.72	15.551	15.5	15.68
Fe_2O_3 incl. FeO	13.074	13.82	12.746	11.5	2.26
Feo					7.41
CaO	7.395	7.36	8.245	4.58	10.85
MgO	4.455	4.99	4.279	7.6	8.35
Na_2O	3.831	3.85	3.696	2.4	2.14
TiO_2	3.122	3.42	3.431	1.1	0.81
K_2O	2.045	1.86	1.897	0.9	0.56
P_2O_5	1.541	1.70	1.720	0.24	0.05
MnO	0.156	0.18	0.172	0.12	0.18

H_2O					0.76
Ba	**1050**	**1700**	**840**		
Sr	**790**	**740**	**800**		
Cl	**560**	**1030**	**1200**		
S	**480**	**590**	**1400**		
V	**0**	**0**	**500**		
Ce	**390**	**380**	**200**		
Zr	**300**	**270**	**400**		
Zn	**170**	**130**	**200**		
Cr	**90**	**0**	**0**		
Rb	**50**	**70**	**44**		
Y	**50**	**40**	**38**		
Nb	**0**	**0**	**25**		

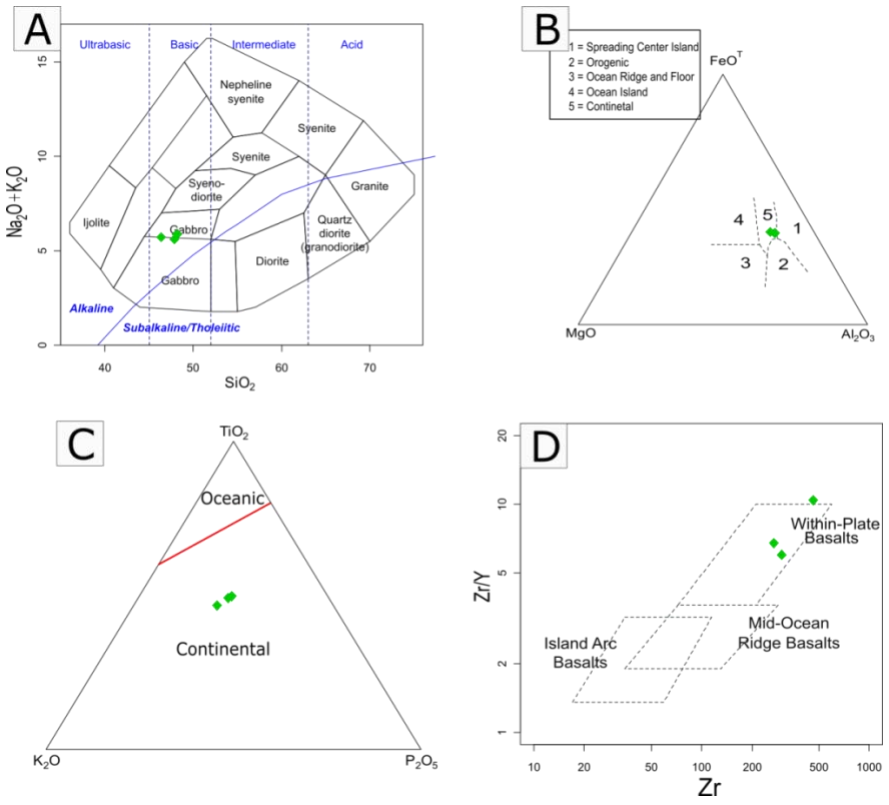

Figure 7 Gabbro samples plotted in A) Na_2O+K_2O vs SiO_2 diagram after Cox et al. (1979); B) MgO-FeO_T- Al_2O_3 after Pearce *et al*. (1977); C) TiO_2–K_2O–P_2O_5 after Pearce et al. (1975); D) Zr/Y vs Zr for basalts after Pearce and Norry (1979).

446 Apatites are versatile geological materials not only useful for geochronological and thermal
447 evolution studies as below but also, for example, to decipher magma-fluid interactions and
448 differentiation (e.g. Harlov 2015). CI-normalized (Anders and Grevesse,1989) Rare Earth
449 Elements values of the 35 apatite crystals from the Caño Viejita gabbro sample Af-7 (**Error!**
450 **Reference source not found.**) analyzed by means of LA-ICP-MS during the U-Pb dating
451 show a strong enrichment mainly of the LREE with a decreasing slope to heavier REE
452 $((Ce/Yb)_{cn}$ of 12-13)) and a moderate negative Eu-anomaly $(2Eu/(Sm+Gd))_{cn}$ of 0.62-0.7),
453 common patterns observed in many apatites. The latter was probably controlled by former or
454 simultaneous plagioclase crystallization (e.g. Rollinson, 1993) much more than the own
455 apatite redox-state. REE-distribution patterns at first glance are similar to apatites from
456 syenites and associated jacupirangites reported by Belousova et al. (2002). However, other
457 parameters differ, like the lower sum of REE between 0.2-0.6wt.%. A slight positive Ce-
458 anomaly $(2Ce/La+Pr)_{cn}$ of 1.1-1.2, Y 328-934ppm, Mn 358-478ppm, Sr 516-747ppm, Th 2.4-
459 6.3ppm, U from 1.1-2.25ppm and mainly radiogenic Pb from 2-8ppm with rather high ^{204}Pb
460 give some clues about the apatite and gabbro crystallization process, using for example the
461 discrimination patterns proposed by Belousova et al. (2002). The Sr/Y values (Sr 516-
462 747ppm / Y 328-934ppm) occupy the granitoid but more the mafic rocks to Fe-ore fields of
463 Belousova et al. (2002). $(Ce/Yb)_{cn}$ of 12-13 and Sum REE 0.2-0.6 wt.% are in the granitoid
464 and near the dolerite field. Sr 516-747ppm/ Mn 358-478ppm correlations are in the larvikites,
465 jacupirangite and iron ore fields, Y 328-934ppm/ Eu/Eu* 62-0.7 occupy the granitoids, mafic
466 rocks and iron ore fields. The absence of observable concurrent phosphate minerals
467 (monazite or xenotime) or garnets which tend to scavenge REE and other incompatible
468 elements as well of zircons explain a good part of this behavior.

469 Thus, both the apatite as the gabbro characteristics hint to a somehow enriched gabbro
470 mantle source.

471

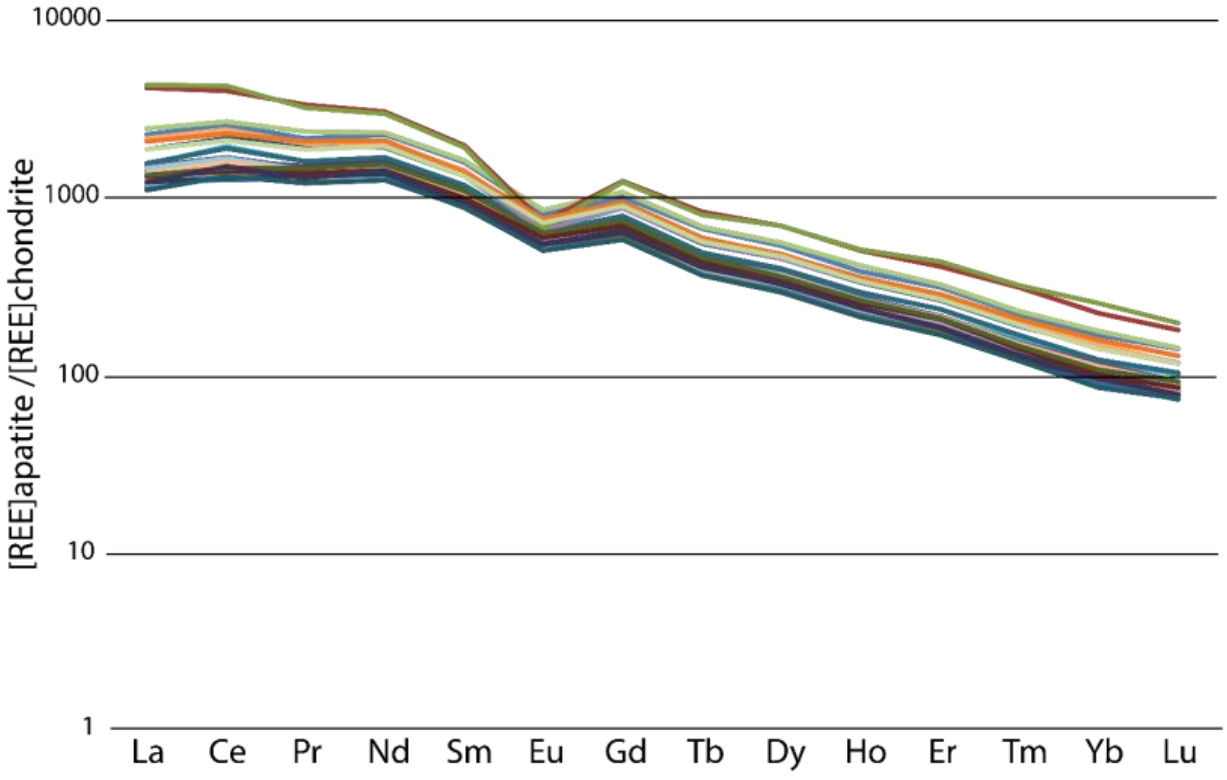

472

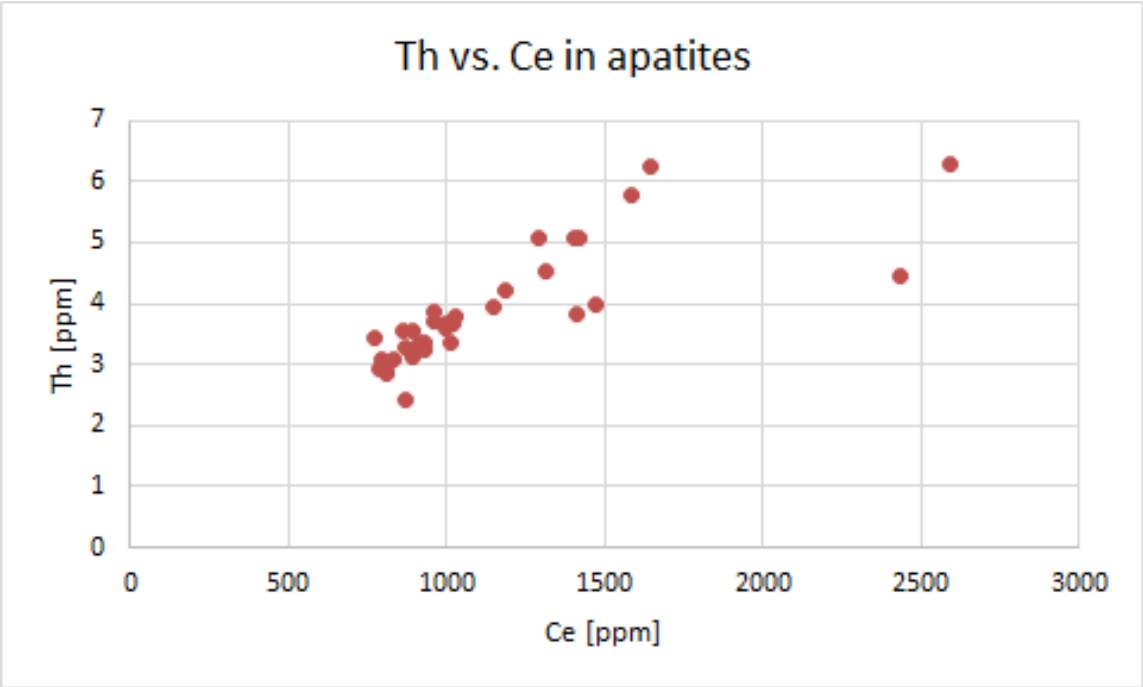

473

474 **Figure 8A** CI-normalized (Anders and Grevesse, 1989 in McDonough and Sun, 1995) REE
475 contents of 35 apatite crystals from Caño Viejita gabbro sample Af-7 showing strong
476 enrichment mainly of LREE with nearly log-linear decrease tendency of heavier REE and a
477 moderate negative Eu-anomaly. **B**: Positive correlation Th vs. Ce in the apatite samples.

4.2 Apatite U-Pb and FT geochronology

As zircon and baddeleyite contents in the gabbro samples are very low and only a few zircon grains were found in thin sections mainly as inclusions inside ilmenite or at the boundary between plagioclase and pyroxene grains, not sufficient material could be obtained for U-Pb geochronology in neither of the Zr-minerals. However, the high amount of good-quality apatite grains allowed applying apatite U-Pb dating. Two samples (Af-1 and Af-7) with large and abundant apatite grains, which exhibit perfect euhedral prism shapes and grain sizes between 100 to 500 µm were selected using binocular, petrological microscope and CL-imaging. CL–images of sample Af-1 exhibit yellow-grayish luminescence free of visible internal structures like cores or zoning (Figure 9).

The U-Pb data of twenty-five apatite grains from this sample Af-1 (Table 4) plotted in a Tera-Wasserburg diagram (Figure 10) show discordant ages with a rather high proportion of common (non-radiogenic) Pb and $^{207}Pb/^{206}Pb$ ratios between 0.38 and 0.49. They yield a lower intercept age of 1001 ± 59 Ma with a $^{207}Pb/^{206}Pb$ initial value of 0.945 (Figure 10). If the discordia is forced to a $^{207}Pb/^{206}Pb$ value of 0.909 ± 0.004, calculated for an age of 1000 ± 50 Ma following the Pb evolution model of Stacey and Kramers (1975), we obtain a similar age, although with lower scattering, of 975 ± 9 Ma (MSWD=0.95) (Figure 10). The weighted average ^{207}Pb-corrected date is in agreement at 979 ± 10 Ma (Figure 10).

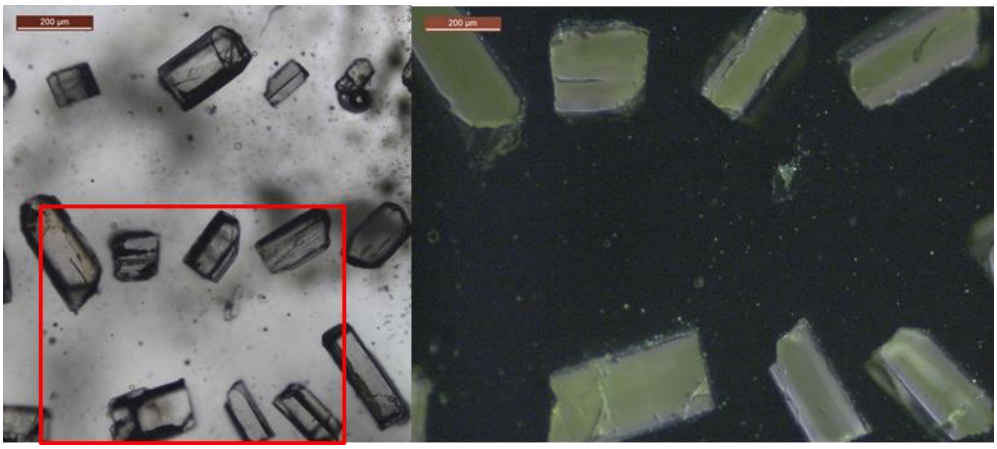

Figure 9 Embedded apatite crystals under the transmitted light microscope (left) and magnified CL-images from Af-1 showing homogeneous yellow-grayish luminescence (right).

U-Pb data of the 35 apatite grains from the second sample (Af-7 in Table 4) yield a lower intercept age of 961 ± 61 Ma with a $^{207}Pb/^{206}Pb$ of 0.864 (Figure 10). The forced regression with an initial common Pb value of 0.909 ± 0.004 yield an age of 1002 ± 21 Ma (Figure 10) coherent with the weighted mean ^{207}Pb-corrected age of 1034 ± 26 Ma (Figure 10). Therefore, the unforced age is coherent with the lower intercept and the corrected age of Af-1 sample. The corrected age (based on Stacey and Kramers 1975 single evolution model) of 1034 ± 26 Ma is the oldest of all obtained ages. In spite of the scatter, both samples share a common history.

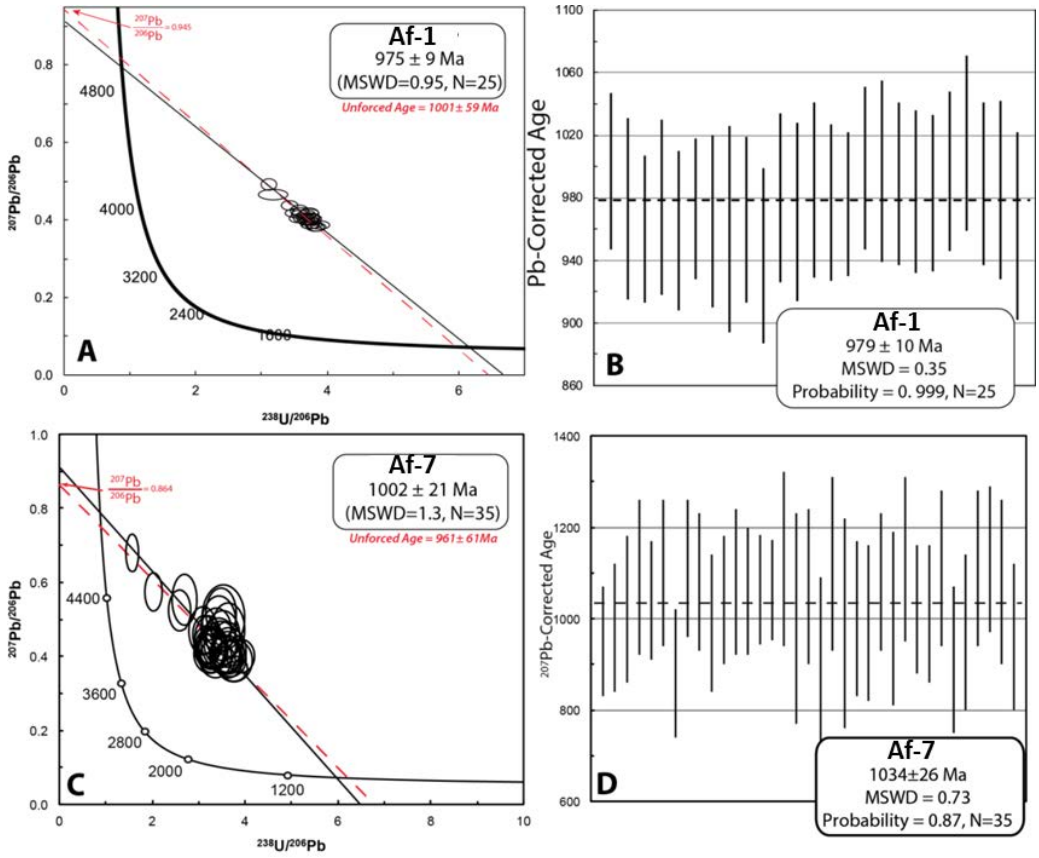

509

510 **Figure 10** Tera–Wasserburg Concordia diagrams and weighted average $_{207}$Pb-corrected
511 ages for the 25 single apatite grains from olivine gabbro sample Af-1 (A+B) and 35 single
512 grains from gabbro Af-7 (C+D).
513

514 A Lower Jurassic (Toarcian) AFT central age of 179.8 ± 9.0 Ma (Figure 11A) based on 33
515 grain analysis could be calculated (Table 4, Figure 11). The chlorine content for the gabbro
516 apatite is 0.28 ± 0.13 wt%, and single grain ages are not related to Cl-content (Figure 11).
517 The spontaneous fission track density is rather low, and only 47 horizontal confined tracks
518 could be measured. The mean track length from this limited data set is short at 11.8 µm, with
519 a large standard deviation of 1.9 µm. An attempt for a thermal history reconstruction must
520 consider that it is based on an absolute minimum of track length information. C-axis
521 projection (Ketcham et al., 2007) of the apatite fission tracks was performed because the data
522 showed anisotropic annealing and follows the model of Donelick et al. (1999) (Figure 11B)

and give a narrower distribution with a c-axis-projected mean length of 13.5 µm. Subsequently, the C-axis-projected length data and the compositional data (i.e. the chlorine-content) were modelled (Figure 11C) with the QTQt software (v5.6.0) (Gallagher, 2012), according to the strategies reported in Van Ranst et al. (2019). After c-axis projection, the mean track length of the sample increased from 11.8 to 13.5 µm and the distribution of the track length histogram was much narrower (Figure 11D).

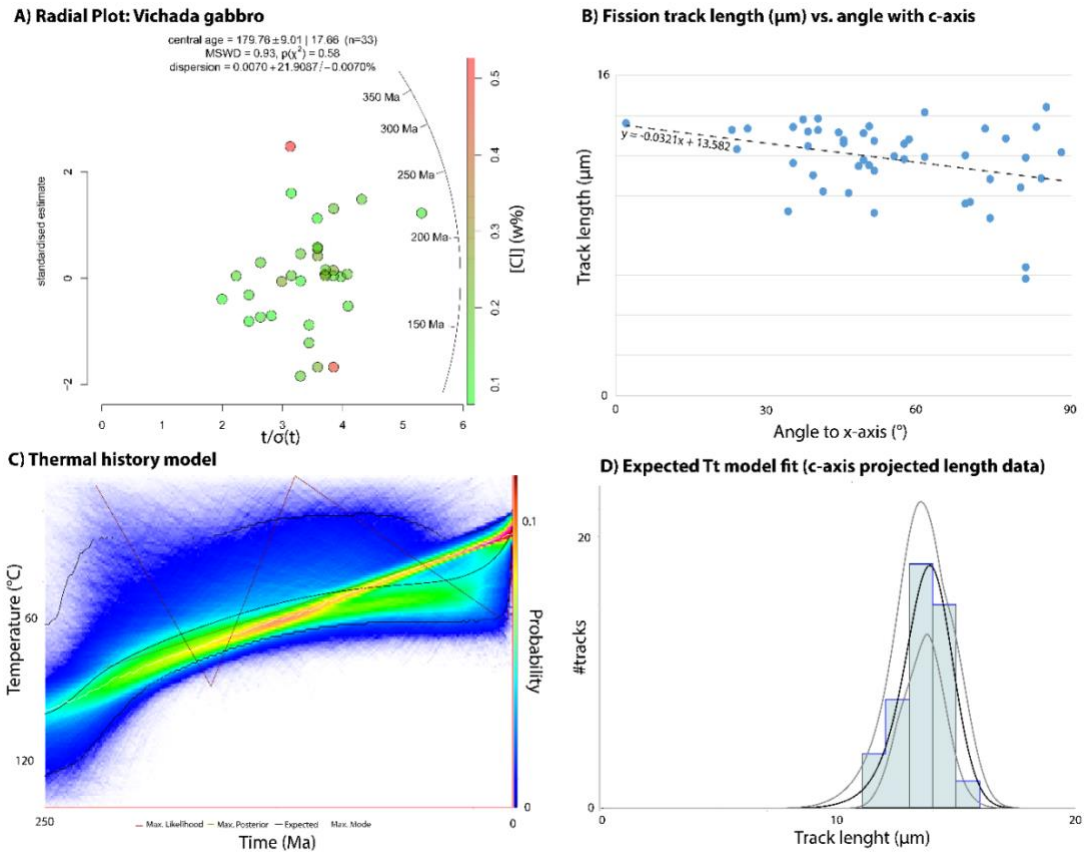

Figure 11 Apatite fission track results of the Vichada gabbro sample Af-7. (A) Radial plot of the analyzed sample with compositional data added as colour scale (using IsoPlotR; (Vermeesch, 2018)). (B) Scatter plot indicating the decreasing trend for apatite fission track length with angle to the c-axis. (C) Thermal history model performed with QTQt (Gallagher, 2012) illustrating the slow cooling through the apatite partial annealing zone (~60°-120°C). (D) Model fit of the expected Tt model (i.e. the black curve in panel C) with the c-axis projected length data.

5. Discussion and conclusions

As the “Caño Viejita” gabbro is limited to the north by a ~50 m thick sedimentary sequence (Figure 4A) which begins north of the intrusion in a creek valley, no clear contact was visible nor a confident extension estimate can be made. Thus, simple field observations did not allow concluding if the gabbro intruded the sediments or if on the contrary the sediments covered the exhumed intrusion at a later stage. This issue will be discussed later in this section.

Lacking quartz and low SiO_2 contents as well as the occurrence of fayalite, pyroxene and bytownite-anorthite as main minerals, point to a mafic to ultramafic primary magma. These observations are consistent with the Al_2O_3 contents from 15.55% to 15.83%, and the low Zr-contents are in agreement with a continental alkaline metaluminous gabbro of Within-Plate characteristics as confirmed by the geochemical-petrotectonic discrimination diagrams (**Error! Reference source not found.**). However, alkali feldspar, mentioned as characteristic of the latter two (Le Maitre et al., 2002), were not found in thin-section nor XRD.

The former seems somewhat in contradiction with the rather low CaO and MgO concentrations and high K_2O and Na_2O content (Table 2). However, the latter can be explained by the influence of continental crust reworking and/or magma mixing as part of an aborted rifting process. The high FeO_{tot} (~11%) and TiO_2 content (3.12% to 3.43%) is expressed in abundant ilmenite and fayalite, and the high P_2O_5 (1.54-1.72%) evidenced in the numerous large apatite crystals may reflect the initial formation of immiscible Ti-Fe-P melts, that, due to their higher density, typically reflect the bottom of mafic intrusions. Interestingly, titanian pyroxene was not found, showing that Ti was hugely scavenged before by ilmenite and to a lesser extent rutile crystallization. The iron incorporation into ilmenite, pyroxene and

562 olivine of very fayalitic composition is also in agreement with the low Mg content. Virtually no
563 magnetite was found in spite of some rutile needles. This all indicates a rather low fO_2 and
564 low liquidus temperature in a highly evolved mafic magmatic system, although still far away
565 from peralkaline miaskitic or much less agpaitic rocks (Marks and Markl, 2017).

566 This work also confirms the utility of apatite trace elements analysis for petrogenetic or
567 exploration purposes (e.g. Mao et al.2016 and references herein). Although the LA-ICP-MS
568 data acquisition was not especially performed for apatite trace elements analysis, using for
569 example the discrimination patterns proposed by Belousova et al. (2002) some light is put on
570 the apatite and gabbro genesis, considering also the absence of observable concurrent
571 phosphate minerals (monazite or xenotime) or garnets which tend to scavenge most of
572 incompatible and RE elements.
573
574 The strong enrichment mainly of the LREE with a nearly log-linear decrease slope to heavier
575 REE $(Ce/Yb)_{cn}$ of 12-13)) and a moderate negative Eu-anomaly $(2Eu/(Sm+Gd))_{cn}$ of 0.62-0.7)
576 (**Error! Reference source not found.**) are common patterns observed in many apatites. The
577 negative Eu-anomaly was probably controlled by former or simultaneous plagioclase
578 crystallization (e.g. Rollinson, 1993) much more than the own apatite redox-state, and would
579 decrease with further magmatic differentiation as observed e.g. in granites. In contrast, mid-
580 ocean ridge gabbro apatites nearly don´t show LREE enrichment in comparison with HREE
581 (see Mao et al. 2016). The dispersion in the apatites of LREE (e.g. La 261- 1030 ppm, Ce
582 770-2590ppm) exceeding for example the dispersion of HREE and Y (328-984ppm) is much
583 more pronounced than the nearly invariant trace elements Sr (516-747ppm) or Mn (358-
584 478ppm). Mn decreases slightly together with Sr, whereas between Y and Sr a strong scatter
585 exists. However, the clear positive correlation between Th and Ce (Fig. 8B) as well as

586 between Y and the REE-sum, evidences their enrichment during the crystallization process.
587 Also both the Th/Ce and Y/REE contents and ratios indicate a more reducing environment
588 (Belousova et al., 2002), whereas for the redox sensitive Mn the picture is not so clear:
589 assuming higher Sr as indicator of less differentiated and more reduced magma, the coupled
590 decrease of Sr and Mn may be caused by the preferred incorporation of Mn^{2+} instead of Mn^{3+}
591 or Mn^{4+} in apatite where it substitutes directly for Ca^{2+} in the two Ca-sites. This assumption is
592 also supported by the slightly positive Ce-anomaly with the preferential incorporation of Ce^{3+}
593 on the $^{[9]}$Ca1-site and the corresponding valence balancing through, e.g. Na^{+}.
594
595 The comparison with the discrimination diagrams of Belousova et al. (2002) give the following
596 picture: The Sr/Y values (Sr 516-747ppm / Y 328-934ppm) occupy the fields of granitoid but
597 more the mafic rocks to Fe-ore fields. $(Ce/Yb)_{cn}$ of 12-13 and Sum REE 0.2-0.6 wt.% are in
598 the granitoid and near the dolerite field. Sr 516-747ppm/ Mn 358-478ppm correlations are in
599 the larvikites, jacupirangite and iron ore fields, Y 328-934ppm/ Eu/Eu* 62-0.7 occupy the
600 granitoids, mafic rocks and iron ore fields. The high P concentrations in the Fe-ore fields like
601 Durango or Kiruna, but also in some of the Fe-Ti-P deposits worldwide as well as the
602 enrichment of K are in agreement with the overlapping of most of these mafic to granitoide
603 and immiscibility magma fields.

604 Neither etching nor the CL images reveal zonation or growth patterns in the apatites. Zircons
605 seem to have crystalized first and were then enclosed by ilmenites or later between nearly
606 coeval plagioclase and pyroxene grains, where also early formed rutile needles are frequent.
607 Altogether, petrologic evidence and main elements as the high K, P, and Na content of the
608 gabbro as well as the apatite trace element geochemistry (high Ce/Yb etc.) plaid against an
609 ophiolite subduction-related origin of the Vichada Viejita Creek gabbro, favoring instead an

610 aborted continental rifting process with relatively low f_{O2}, little water (no amphiboles nor mafic
611 pegmatites) and low Cl content. As fluxing agent, phosphorous may have played an important
612 role in the system. Some of the gabbro whole-rock and apatite geochemical characteristics
613 hint to sediment or continental crust recycling, but also to magma mixing with some
614 lamprophyre, carbonatite or anorthosite associated Fe-Ti-P signatures.
615
616 The two U-Pb principal ages obtained from 25 (Af-1) and 35 (Af-7) apatite grains,
617 respectively, are discordant and show a scattering of individual grain ages. They yield lower
618 intercept ages of 1001 ± 59 Ma (Af-1) and 961 ± 61 Ma (Af-7) with a $^{207}Pb/^{206}Pb$ initial value
619 of 0.945 (Figure 10). Adjusting them to the Pb evolution model of Stacey and Kramers (1975),
620 we obtain similar ages of 975 ± 9 Ma (Af-1) and 1002 ± 21 Ma (Af-7), with Af-1 showing no
621 lower scattering. This rather broad range in ages may have two principal reasons: either
622 analytical-procedural based dispersion, or geological-mineralogical factors and their
623 interaction. The low scatter of analytical data of the different standard apatites used during
624 measurement suggest a rather stable instrument configuration and no measuring
625 disturbance. However, apart from differences between the two sample groups from different
626 parts of the gabbro also the different analytic procedures have contributed, as in the second
627 case also AFT data were to be obtained. Among the geological-mineralogical factors, first the
628 rather high proportion of common (non-radiogenic) Pb is to be mentioned, inhomogeneities of
629 HFSE incorporation during the crystallization process as also evidenced by the high REE
630 scattering in the apatite samples from gabbro Af-7; the homogeneous CL-images of apatites
631 from Af-1 suggest no zonation during apatite growth. Although the U-Pb apatite closure
632 temperature of ~500°C is much lower than for zircons (Chew and Spikings, 2015) and than
633 the magma emplacement temperature (>1000 °C or perhaps lower due to continental
634 contaminants, fluids and high P) neither diffusion effects during the cooling process nor later

635 thermal peaks can be ruled out. So there is no doubt that both apatite U-Pb ages show a
636 common history related to the magmatic emplacement and cooling process and much more
637 unlikely posterior thermal events. Small mafic bodies as the Viejita Creek gabbro tend to
638 solidify and cool below the apatite closure temperature in less than ~100 years. Additionally,
639 the absence of metamorphic overprinting signs both in rocks and thin-sections, rule out
640 stronger posterior thermal events.

641 This Early Neoproterozoic Viejita Creek gabbro exhibit strong similarities with other mafic
642 bodies outcropping hundreds of kilometers to the south near to the Vaupés and Apaporis
643 rivers extending at least until Brazil (Figure 2). Their radiometric ages are considerably older
644 (100-200 Ma), however, but also were obtained by other radiometric methods (K/Ar + Rb/Sr).
645 The Rb/Sr isochrons are considered to give too low regional ages with very large error
646 margins (Kroonenberg et al., 2016). Such a large time difference only caused because of
647 analytical differences is not very probable, but we don´t have enough elements for a definite
648 conclusion, at the moment.
649
650 The reported time window of Neoproterozoic mafic magmatism in the western Amazonian
651 craton span from 940 to 1225 Ma (Table 1). To the East (Brazilian Taraira) are some of the
652 youngest reported ages ~ 940 to 980 Ma (Tassinari, 1996), and moreover there seems to be
653 a South-to-North trend from older to younger magmatism, possibly indicating several cycles
654 of cortical opening and closing in different parts of the craton. About 200km to the East of our
655 study area, the youngest known intracratonic magmatic rocks in the NW Amazonian Craton,
656 the Nepheline Syenite of San José del Guaviare, of Neoproterozoic-Ediacaran to Cambrian
657 ages of ~578 Ma (Mejia et al., 2012) and biotite K/Ar and Rb/Sr cooling ages of 445 – 495 Ma
658 (Pinson et al., 1962) outcrops over > 10 square kilometers. Recently obtained own LA-ICP-

MS U-Pb zircon ages of ~609 Ma in the southern extension near Jordan (Franco et al., 2018; Muñoz Rocha et al., 2019) suggest a long emplacement and cooling history for this large body. Further west, no intracratonic intrusions are reported until now. Anyhow, the San José del Guaviare Nepheline Syenite is another indication of tectonic reactivation of structural weakness zones in the crust, possibly representing older suture or rift zones. Whilst in the case of the older Viejita Creek gabbro the Grenvillian orogeny as partial response to the Rodinia Supercontinent assembly some 1 Ga ago was the most likely cause producing a distinctive enrichment of Ti, K, P and REEs in apatites from the mantel-derived magma, the magmatic differentiation of the Nepheline Syenite, coeval but not necessarily caused by the Pan-African-Braziliano orogeny, produced more agpaitic rocks and characteristic minerals such as large zircon crystals.

Also other alkaline to carbonatitic intrusions in the NW Amazonian Craton may be related to Grenvillian sequences s.l. (Cordani et al., 2010) or later events. The Nepheline Syenites of the Muri Alkaline Complex are dated between 1026 ± 28 Ma (Issler et al., 1975) and 1090 Ma (Kroonenberg et al., 2016). For the Nb-rich Seis Lagos Carbonatite Complex (SLCC) in Brazil near to the Colombian border, Rossoni et al. (2017) established an U-Pb zircon maximum age of 1328 Ma, at the very beginning of the Grenvillian, but other authors attribute much younger ages, which span from the Cambrian to the Triassic (Pinheiro et al., 1976). For the diamondiferous Guaniamo layered kimberlite sheets in Venezuela, ages between 840 and 710 Ma are claimed (Channer et al., 2001).

These examples illustrate sufficiently, how much work is still to be done in the often difficult to access and covered areas of the Amazonian Craton in order to get an indisputable and generally accepted reconstruction of the Craton´s history. Much better defined in this sense

684 are the anorogenic granites such as the Parguaza Rapakivi Batholith from 1392 ± 5 Ma to
685 1402 ± 2 Ma in Colombia (Bonilla et al., 2013), although this is younger than the ages of the
686 batholith reported in Venezuela of ~1545 Ma. The comparable felsic Matraca rapakivi
687 granites (Bonilla et al., 2016) seem to have a narrow correlation with U-Pb LA-ICP-MS ages
688 of 1381 – 1343 Ma from pegmatitic monazite and xenotime of the Chorrobocon colluviums in
689 the Colombian Guainía Department (Franco et al., 2019), where granitic intrusions and
690 associated mineralizations prove to be much more prominent than in other portions of the
691 Mitú Complex (Bonilla et al., 2019).
692
693 With respect to the relation between the intrusive and the sandstone cover mentioned in the
694 beginning of this chapter, another gabbro outcrop ~10km to the west of the study area (Cerro
695 Siare, Figure 3) may give some hints. This gabbro consists of 55-60% plagioclase, 3-5%
696 pyroxene, 2-8% olivine and 25-30% chlorite and crosscuts as a vertical dike the sandstone
697 sequence, as reported by Franco (2002). Initially, Vesga & Castillo (1972) described the
698 sedimentary sequence informally as “Raudales-Iteviare Sandstone”. However, in the updated
699 Colombian Geological Map (Gómez Tapias et al., 2015) these sediments are now correlated
700 with the Ordovician Araracuara Formation (without reported ages). But the detailed
701 description of this unit by Franco (2002), who recognized a detailed column of 372 m thick
702 sub-arkoses to quartz sandstones and conglomeratic sandstones as part of the Mapiripana
703 Formation of Mesoproterozoic age is very convincing, although much more study including
704 field work and geochronology has to be done for a final conclusion. The Mapiripana
705 Formation as well as the La Pedrera Formation are more likely part of a northern extension of
706 the Tunui Group (Pinheiro et al., 1976), which also forms the gold-rich Naquén and
707 Caranacoa mountains of Mesoproterozoic age. All of them seem to represent molasse
708 deposits of different oogenesis eroded long after the consolidation of the Roraima Formation.

709 In the latter, detrital zircon U-Pb ages of 2171-1958 Ma (Santos et al., 2003) indicate a Trans-
710 Amazonian Orogeny origin of the sediments (Kroonenberg et al., 2016), with more or less
711 well developed metamorphic overprinting. The series of Neoproterozoic gabbros could have
712 intruded and cut rocks of the Mitu Complex (Bonilla et al., 2019; Galvis et al., 1979; López et
713 al., 2007; Rodríguez et al., 2011) as part of the 1.80-1.55 Ga Rio Negro-Juruena
714 Geochronological Province (Figure 2) in Colombia (Tassinari, 1996; Tassinari and
715 Macambira, 1999) and also the 1.87-1.5 Ga Roraima-Formation-like sedimentary covers
716 (Tunui Group). The oldest metamorphic overprint of those sediments was dated at ~1.3 Ga
717 and related with the incipient Grenvillian event (Kroonenberg and de Roever, 2010).
718

719 The Amazonian Craton as a whole seems to have behaved as a rigid block where
720 deformation mostly concentrated along pre-existing major shear zones that could accompany
721 the uplift of the intervening blocks, the development of rift basins, emplacement of bi-modal
722 magmatic suites and extensional fractures which were filled by mafic dike swarms (Cordani et
723 al., 2010) or intrusions. This suggests that granitic, mafic and syn-sedimentary sequences of
724 Grenvillian age outcropping in the Colombian Rio Negro Juruena Province would be the
725 result of different stages of intraplate rifting and shearing induced by continent-continent
726 collision (Putumayo Orogen and Sunsás belt). This tectonic regime hence also created easier
727 pathways for the ascent of magmas. The Viejita Creek Gabbro represents such a mafic body
728 associated with intraplate rifting, as a response to the Rodinia Supercontinent assembly. This
729 mafic intrusion contains a rare lithology in this part of the Amazonian Craton where felsic
730 rocks of the Rio Negro-Juruena province predominate. This points to a mantle origin with high
731 crustal influence or magma mixing and rifting caused by significant collisions like those
732 assumed to have occurred during the Grenvillian.

733

734 The NE-SW and NW-SE structural trends in the Eastern Colombian basement are visible as
735 main lineaments all over the Amazonian Craton. They were interpreted mainly as the result of
736 compression during Mesoproterozoic accretion stages (Galvis et al., 1979; Tassinari and
737 Macambira, 1999) such as the Rondonian-San Ignacio orogeny, or the Sunsás orogeny
738 (Cordani et al., 2010). In this context, our data and other research suggest that the mafic
739 intrusion occurred related with a NW-SE trending intra plate or rifting event some 970 Ma ago
740 (or slightly before) affecting the Rio Negro Juruena Province. This may have been associated
741 with the Putumayo Orogeny (Ibañez et al., 2015) proposed for the late phases of the

742 Amazonia-Baltica-Laurentia collision. Possibly in this context or earlier, a sedimentary basin
743 opened, accommodating the deposition of sediments during the late Mesoproterozoic.
744
745 In relation to the gabbro's exhumation process, the apatite fission track central age of 179.8 ±
746 9.0 Ma extracted from 47 measurements of high-quality apatite crystals (Figure 11), allow
747 some preliminary conclusions for developing a thermal history model. The time-temperature
748 path with the highest probability suggests continuous and slow cooling through the Apatite
749 Partial Annealing zone during the Meso- and Cenozoic, since the Jurassic.
750
751 The understanding of the thermal history of the Colombian part of the Amazonian craton is in
752 its beginning and requires more thermochronological data. Apatite and zircon fission track
753 thermochronology until now focused mainly on the Andes Cordillera, where mostly Andean,
754 i.e. Cenozoic ages are retrieved from basement rocks (Amaya et al., 2017; Parra et al., 2009;
755 Villagómez and Spikings, 2013). The analyzed samples exhumated ~400km southeastwards
756 of the Andean thrust front or Borde Llanero Fault System (Restrepo-Pace and Cediel, 2010),
757 did not cool rapidly as would result from an Andean orogeny uplift, but rather experienced a
758 gradual, slow cooling through the 120°-60°C temperature window (Apatite Partial Annealing
759 Zone). This slow cooling occurred in the regional context of Mesozoic extension during which
760 backarc and marginal basins developed in western South America (Coney and Evenchick,
761 1994; Dalziel, 1986; Mpodozis and Ramos, 1989). The source-material for these basins were
762 predominantly clastic sediments originating from the cratonic lithosphere (e.g. Horton, 2018
763 and references therein). Further possible geochronological evidence for the gradual slow
764 erosion of the Grenvillian remnants are found in the Llanos basin to the west of our study
765 area, in which the 950-1050 Ma age population is one of the most dominant zircon U-Pb age

766 populations of the sedimentary record from the Paleozoic to the Late Cenozoic (Horton et al.,
767 2010).
768
769 ## 6. Acknowledgements
770 The first author wishes to acknowledge the PhD-studies grant received by COLCIENCIAS.
771 SN got funds through a PhD fellowship from the Research Foundation Flanders (FWO).
772 Sampling and analysis were also possible due to Zeze Amaya, Ana Elena Concha and
773 others. Two anonymous reviewers helped to improve the manuscript on important aspects
774
775 ## 7. Bibliography
776
777 Almeida, M.E., Larizzatti, J.H., 1996. Geologia e petrografia da Suíte Intrusiva Içana no alto
778 rio Uaupés, Estado do Amazonas, Brasil., in: SBG, Congresso Brasileiro de Geologia,
779 39. Balneário de Camboriú, pp. 399–403.
780 Almeida, M.E., Luzardo, R., S.S., P., Oliveira, M.A., 2004. Folha NA.19-Pico da Neblina. In:
781 Schobbenhaus, C., Gonçalves, J.H., Santos, J.O.S., Abram, M.B., Leão Neto, R., Matos,
782 G.M.M., Vidotti, R.M., Ramos, M.A.B., Jesus, J.D.A. de. (eds.). Carta Geológica do
783 Brasil ao Milionésimo. Brasília.
784 Almeida, M.E., Macambira, M.J.B., Scheller, T., 1997. Içana Intrusive Suite: age
785 207Pb/206Pb (zircon evaporation) of muscovite bearing granite, Amazonas State, Brazil,
786 in: South American Symposium on Isotope Geology, 1. Campos do Jordao, pp. 31–33.
787 Anders, E., Grevesse, N., 1989. Abundances of the elements: Meteoric and solar.
788 Geochimica et Cosmochimica Acta 53, 197–214.
789 Amaya, S., Zuluaga, C.A., Bernet, M., 2017. New fission-track age constraints on the
790 exhumation of the central Santander Massif: Implications for the tectonic evolution of the

Northern Andes, Colombia. Lithos 282–283, 388–402. https://doi.org/https://doi.org/10.1016/j.lithos.2017.03.019

Belousova, E.A., Griffin, W.L., O'Reilly, S.Y., Fisher, N.I., 2002. Apatite as an indicator mineral for mineral exploration: trace-element compositions and their relationship to host rock type. Journal of Geochemical Exploration 76, 45–69. https://doi.org/10.1016/S0375-6742(02)00204-2

Bettencourt, J.S., Tosdal, R.M., Leite Jr., W.B., Payolla, B.L., 1999. Mesoproterozoic rapakivi granites of the Rondonia Tin Province, southwestern border of the Amazonian craton, Brazil-I. Reconnaissance U-Pb geochronology and regional implications. Precambrian Res. 95, 41–67. https://doi.org/10.1016/S0301-9268(98)00126-0

Bonilla, A., Frantz, J.C., Charão-Marques, J., Cramer, T., Franco, J.A., Mulocher, E., Amaya-Perea, Z., 2013. Petrografía, Geoquímica y Geocronología del Granito de Parguaza en Colombia. Bol. Geol. 35, 83–104.

Bonilla, A., Frantz, J.C., Charão-Marques, J., Cramer, T., Franco, J.A., Amaya-Perea, Z., 2016. Magmatismo rapakivi en la cuenca media del río Inírida, departamento de Guainía, Colombia. Bol. Geol. 38, 17–32. https://doi.org/http://dx.doi.org/10.18273/revbol.v38n1-2016001

Bonilla, A., Cramer, T., Poujol, M., Cano, H., Franco, J.A., Amaya, Z., 2019. Petrografía, geoquímica y geocronología U / Pb en circones de rocas ígneas y metamórficas a lo largo del Río Cuiarí en el sur del Departamento de Guainía, Colombia. Bol. Geol. 41, 55–84. https://doi.org/10.18273/revbol.v41n1-2019003

Cardona, A., Chew, D., Valencia, V.A., Bayona, G., Mišković, A., Ibañez, M., 2010. Grenvillian remnants in the Northern Andes: Rodinian and Phanerozoic paleogeographic perspectives. J. South Am. Earth Sci. 29, 92–104. https://doi.org/10.1016/j.jsames.2009.07.011

816 Cardona, A., Valencia V, A., Bayona, G., Duque, J., Ducea, M., Gehrels, G., Jaramillo, C.,
817 Montes, C., Ojeda, G., J., R., 2011. Early-subduction-related orogeny in the northern
818 Andes: Turonian to Eocene magmatic and provenance record in the Santa Marta Massif
819 and Rancheria Basin, northern Colombia. Terra Nov. 23, 26–34.
820 https://doi.org/doi:10.1111/j.1365-3121.2010.00979.x
821 Carneiro, M.C.R., Nascimento, R.S.C., Almeida, M., Trindade, I.R., Salazar, C.A., 2017a.
822 Leucognaisses alcalinos no Dominio Imeri, Provincia Rio Negro-NW do Estado do
823 Amazonas. https://doi.org/10.13140/RG.2.2.19376.35840
824 Carneiro, M.C.R., Nascimento, R.S.C., Almeida, M.E., Salazar, C.A., Trindade, I.R. da,
825 Rodrigues, V. de O., Passos, M.S., 2017b. The Cauaburi magmatic arc: Litho-
826 stratigraphic review and evolution of the Imeri Domain, Rio Negro Province, Amazonian
827 Craton. J. South Am. Earth Sci. 77, 310–326.
828 https://doi.org/10.1016/j.jsames.2017.06.001
829 Channer, D.M.D., Egorov, A., Kaminsky, F., 2001. Geology and structure of the Guaniamo
830 diamondiferous kimberlite sheets, south-west Venezuela. Rev. Bras. Geociências 31,
831 615–630. https://doi.org/10.25249/0375-7536.2001314615630
832 Chew, D.M., Babechuk, M.G., Cogné, N., Mark, C., O'Sullivan, G.J., Henrichs, I.A., Doepke,
833 D., McKenna, C.A., 2016. (LA,Q)-ICPMS trace-element analyses of Durango and
834 McClure Mountain apatite and implications for making natural LA-ICPMS mineral
835 standards. Chem. Geol. 435, 35–48.
836 https://doi.org/https://doi.org/10.1016/j.chemgeo.2016.03.028
837 Chew, D.M., Spikings, R.A., 2015. Geochronology and Thermochronology Using Apatite:
838 Time and Temperature, Lower Crust to Surface. Elements 3, 189–194.
839 Cochrane, R., Spikings, R.A., Chew, D., Wotzlaw, J.F., Chiaradia, M., Tyrrell, S., Schaltegger,
840 U., Van der Lelij, R., 2014. High temperature (>350°C) thermochronology and

841 mechanisms of Pb loss in apatite. Geochim. Cosmochim. Acta 127, 39–56.
842 https://doi.org/10.1016/j.gca.2013.11.028
843 Cogné, N., Chew, D. M., Donelick, R. A. Ansberque, C., 2019. LA-ICP-MS apatite fission
844 track dating: A practical zeta-based approach,Chemical Geology, In
845 Press. https://doi.org/10.1016/j.chemgeo.2019.119302
846 Coney, P.J., Evenchick, C.A., 1994. Consolidation of the American Cordilleras. J. South Am.
847 Earth Sci. 7, 241–262. https://doi.org/https://doi.org/10.1016/0895-9811(94)90011-6
848 Cordani, U.G., Fraga, L.M., Reis, N., Tassinari, C.G., Brito-Neves, B.B., 2010. On the origin
849 and tectonic significance of the intra-plate events of Grenvillian-type age in South
850 America: A discussion. J. South Am. Earth Sci. 29, 143–159.
851 https://doi.org/10.1016/j.jsames.2009.07.002
852 Cordani, U.G., Sato, K., Sproessner, W., Fernandes, F.S., 2016. U-Pb zircon ages of rocks
853 from the Amazonas Territory of Colombia and their bearing on the tectonic history of the
854 NW sector of the Amazonian Craton, Brazilian Journal of Geology.
855 https://doi.org/10.1590/2317-4889201620150012
856 Cordani, U.G., Tassinari, C.C.G., Teixeira, W., Basei, M.A.S., Kawashita, K., 1979. Evolução
857 tectônica da Amazônia com base nos dados geocronológicos. Actas. PP - Ciudad Arica.
858 Cordani, U.G., Teixeira, W., D'Agrella-Filho, M.S., Trindade, R.I., 2009. The position of the
859 Amazonian Craton in supercontinents. Gondwana Res. 15, 396–407.
860 https://doi.org/10.1016/j.gr.2008.12.005
861 Cox, K.G., Bell, J.D., Pankhurst, R.J., 1979. The interpretation of igneous rocks, George All.
862 ed. London.
863 Dall'Agnol, R., Costi, H.T., Leite, A.A. da S., de Magalhães, M.S., Teixeira, N.P., 1999.
864 Rapakivi granites from Brazil and adjacent areas. Precambrian Res. 95, 9–39.
865 https://doi.org/10.1016/S0301-9268(98)00125-9

866 Dalziel, I.W.D., 1986. Collision and Cordilleran orogenesis: an Andean perspective. Geol.
867 Soc. London, Spec. Publ. 19, 389–404. https://doi.org/10.1144/GSL.SP.1986.019.01.22
868 Departamento Nacional da Producäo Mineral, 1976. Folha NA. 19 Pico da Neblina: geología,
869 geomorfología, pedología, vegetaeäo e uso potencial da terra. Proj. Radambras. -
870 Levant. Recur. Nat. 11, 380.
871 Dewanckele, J., De Kock, T., Fronteau, G., Derluyn, H., Vontobel, P., Dierick, M., Van
872 Hoorebeke, L., Jacobs, P., Cnudde, V., 2014. Neutron radiography and X-ray computed
873 tomography for quantifying weathering and water uptake processes inside porous
874 limestone used as building material. Mater. Charact. 88, 86–99.
875 https://doi.org/10.1016/j.matchar.2013.12.007
876 Donelick, R.A., Ketcham, R.A., Carlson, W.D., 1999. Variability of apatite fission-track
877 annealing kinetics: II. Crystallographic orientation effects. Am. Mineral. 84, 1224–1234.
878 https://doi.org/10.2138/am-1999-0902
879 Donelick, R.A., O'Sullivan, P.B., Ketcham, R.A., 2005. Apatite fission-track analysis, Low
880 Temperature Thermochronology: Techniques, Interpretations, and Applications. Reviews
881 in Mineralogy and Geochemistry.
882 Franco, D., 2002. Estratigrafía, petrografía y análisis de proveniencia de la secuencia
883 sedimentaria aflorante en la Serranía de Mapiripana, departamentos de Guainía y
884 Vichada. Thesis. Universidad Nacional de Colombia.
885 Franco, J.A., Muñoz, J.A., Piraquive, A., Bonilla, A., Cramer, T., Campos, H., 2018.
886 Geochronology of the Nepheline Syenite of el Jordán, Guaviare Colombia, evidences of
887 Neoproterozoic- Cambrian intraplate magmatism and its implications during Pan- African
888 tectonics in western Gondwana., in: Geophysical Research Abstracts Vol. 20, EGU2018-
889 10861, 2018 EGU General Assembly 2018. Vienna, p. 10861.
890 Franco, J.A., Cramer, T., Bonilla, A., 2019. Critical minerals in Colombia, characteristics, ages

and potential of Ti-Nb-Ta, REE and U-Th mineralizations in Cerro Espina, Guainía. *In progress.*

Gallagher, K., 2012. Transdimensional inverse thermal history modeling for quantitative thermochronology. J. Geophys. Res. Solid Earth 117. https://doi.org/10.1029/2011JB008825

Galvis, J., Huguett, A., Ruge, P., 1979. Geología de la Amazonía Colombiana. Bol. Geológico.

Gansser, A., 1954. The Guiana Shield (S. America) Geological Observations. Eclog. Geol. Helvet 47, 77–112.

Gaudette, H.E., Mendoza, V.S., Hurley, P.M., Fairbairn, H.W., 1978. Geology and age of the Parguaza rapakivi granite, Venezuela. Bull. Geol. Soc. Am. 89, 1335–1340. https://doi.org/10.1130/0016-7606(1978)89<1335:GAAOTP>2.0.CO;2

Gómez Tapias, J., Montes Ramírez, N.E., Nivia Guevara, Á., Diederix, H. (Eds.), 2015. Atlas Geológico de Colombia, Plancha 5-15AGC 2015. Scale 1:500 000. Servicio Geológico Colombiano, Bogotá.

Harlov, D.E., 2015. Apatite: A Fingerprint for Metasomatic Processes. Elements 11, 171–176. https://doi.org/10.2113/gselements.11.3.171

Hasebe, N., Barbarand, J., Jarvis, K., Carter, A., Hurford, A., 2004. Apatite fission-track chronometry using laser ablation ICP-MS. Chem. Geol. 207, 135–145. https://doi.org/10.1016/j.chemgeo.2004.01.007

Hoffman, P.F., 1991. Did the Breakout of Laurentia Turn Gondwanaland Inside-Out? Science (80-.). 252, 1409–1412. https://doi.org/10.1126/science.252.5011.1409

Horton, B. K., 2018. Tectonic Regimes of the Central and Southern Andes: Responses to Variations in Plate Coupling During Subduction. Tectonics 37, 402–429. https://doi.org/doi:10.1002/2017TC004624

916 Horton, B.K., Parra, M., Saylor, J.E., Nie, J., Mora, A., Torres, V., Stockli, D.F., Strecker,
917 M.R., 2010. Resolving uplift of the northern Andes using detrital zircon age signatures.
918 GSA Today 20, 4–9. https://doi.org/10.1130/GSATG76A.1
919 Huguett, A., 1977. Geología de la Comisaría del Guainía, Colombia, en base a imágenes de
920 radar, Carta Técnica. Ministerio de Minas y Energía, Instituto Nacional de
921 Investigaciones Geologico-Mineras,Proyecto Radargramétrico del Amazonas, Bogotá.
922 Hurford, A.., Green, P.., 1983. The zeta age calibration of fission-track dating. Chem. Geol. 1,
923 285–317.
924 Ibañez, M., 2010. New U-Pb geochronological insights into the Proterozoic tectonic evolution
925 of Northwestern South America: The Mesoneoproterozoic Putumayo Orogen of
926 Amazonia and implications for Rodinia Reconstructions. The University of Arizona.
927 Ibáñez-Mejía M, Ruiz J, Valencia VA, Cardona A, Gehrels GE, Mora AR., 2011. The
928 Putumayo Orogen of Amazonia and its implications for Rodinia reconstructions: new U–
929 Pb geochronological insights into the Proterozoic tectonic evolution of northwestern
930 South America. Precambrian Res 191:58–77
931 Ibañez, M, Pullen, A., Arenstein, J., Gehrels, G.E., Valley, J., Ducea, M.N., Mora, A.R.,
932 Pecha, M., Ruiz, J., 2015. Unraveling crustal growth and reworking processes in
933 complex zircons from orogenic lower-crust: The Proterozoic Putumayo Orogen of
934 Amazonia. Precambrian Res. 267, 285–310.
935 https://doi.org/10.1016/j.precamres.2015.06.014
936 Issler, R.., de Lima, R.M.., Montalvao, G.., 1975. Magmatismo alcalino no craton Guianes, in:
937 Anais Decima Conferencia Geologica Interguianas, Belem Do Para, Brazi. pp. 103–122.
938 Janousek, V., Farrow, C.M., Erban, V., 2008. Geochemical Data Toolkit in R, version for
939 Windows.
940 Ketcham, R., Carter, A., Donelick, R., Barbarand, J., Hurford, A.J., 2007. Improved modeling

941 of fission-track annealing in apatite. Am. Mineral. 92, 799–810.
942 https://doi.org/10.2138/am.2007.2281
943 Ketcham, R.A., Donelick, R.A., Carlson, W.D., 1999. Variability of apatite fission-track
944 annealing kinetics: III. Extrapolation to geological time scales. Am. Mineral. 84, 1235–
945 1255. https://doi.org/10.2138/am-1999-0903
946 Klemme, S., John, T., Wessels, M., Kusebauch, C., Berndt, J., Rohrbach, A., Schmid-
947 Beurmann, P., 2013. Synthesis of trace element bearing single crystals of Chlor-Apatite
948 (Ca5(PO4)3Cl) using the flux growth method. Chem. Cent. J. 7, 56.
949 https://doi.org/10.1186/1752-153X-7-56
950 Kroonenberg, S. B., 2019. The Proterozoic Basement of the Western Guiana Shield and the
951 Northern Andes. In F. Cediel and R. P. Shaw (Eds.), Geology and Tectonics of
952 Northwestern South America (pp. 115–192). Cham: Springer International Publishing.
953 https://doi.org/10.1007/978-3-319-76132-9_3
954 Kroonenberg, S.B., de Roever, E.W.F., Fraga, L.M., Reis, N.J., Faraco, T., Lafon, J.-M.,
955 Cordani, U., Wong, T.E., 2016. Paleoproterozoic evolution of the Guiana Shield in
956 Suriname: A revised model. Netherlands J. Geosci. 95, 491–522.
957 https://doi.org/10.1017/njg.2016.10
958 Kroonenberg, S.B., de Roever, E.W.F., 2010. Geological Evolution of the Amazonian Craton,
959 in: Hoorn, C., Wesseling, F.. (Eds.), Amazonia, Landscape and Species Evolution: A
960 Look into the Past. Wiley-Blackwell Publishing Ltd., Oxford, UK, pp. 9–28.
961 https://doi.org/10.1002/9781444306408.ch2
962 Mao, M., Rukhlov, A.S., Rowins, S.M., Spence, J., Coogan, L.A., 2016. Apatite Trace
963 Element Compositions: A Robust New Tool for Mineral Exploration. Economic Geology
964 111, 1187–1222. https://doi.org/10.2113/econgeo.111.5.1187
965 Le Maitre, R., 1976. The Chemical Variability of some Common Igneous Rocks. J. Petrol. 17,

589–598. https://doi.org/10.1093/petrology/17.4.589

Le Maitre, R., Streckeisen, A., Zanettin, B., Bas, M.J. Le, Bonin, B., Bateman, P., 2002. Igneous Rocks: A Classification and Glossary of Terms: Recommendations of the International Union of Geological Sciences Subcommission on the Systematics of Igneous Rocks. Cambridge University Press, Cambridge.

López, J., Khurama, S., Bernal, L., Cuellar, M., 2007. EL Complejo Mitú: Una Nueva Perspectiva. Memorias XI Congr. Colomb. Geol. 1–16.

Marks, M.A.W., Markl, G., 2017. A global review on agpaitic rocks. Earth-Science Rev. 173, 229–258. https://doi.org/10.1016/j.earscirev.2017.06.002

McDonough, W.., Sun, S., 1995. The composition of the Earth. Chem. Geol. 120, 223–253. https://doi.org/10.1016/0009-2541(94)00140-4

McDowell, F.W., McIntosh, W.C., Farley, K.A., 2005. A precise 40Ar–39Ar reference age for the Durango apatite (U–Th)/He and fission-track dating standard. Chem. Geol. 214, 249–263. https://doi.org/https://doi.org/10.1016/j.chemgeo.2004.10.002

Mejia, M.I.A., Garcia, G.Z., Martens, U., 2012. Caracterización petrográfica, geoquímica y edad de la sienita nefelínica de san josé del guaviare. Bol. Geol. 34, 15–26.

Mielke, J.E., 1979. Composition of the Earth's Crust and Distribution of the Elements, in: Siegel, F. ed., Review of Research on Modern Problems in Geochemistry - Earth Science Series 16: Paris, International Association for Geochemistry and Cosmochemistry, p. 13–37.

Mpodozis, C., Ramos, V., 1989. The Andes of Chile and Argentina, in: Geology of the Andes and its Relation to Hydrocarbon and Mineral Resources. Earth Sci. Ser. 11, 59–90.

Muñoz Rocha, J.A., Piraquive, A., Franco Victoria, J.A., Bonilla, A., Peña Urueña, L.M., Cramer, T., Rayo Rocha, L. del P., Villamizar Escalante, N., 2019. Megacircones ediacáricos de la sienita nefelínica de San José del Guaviare y su potencial como

991 material de referencia para datación U/Pb mediante LA-ICP-MS. Boletín Geológico 45,
992 5–22. https://doi.org/10.32685/0120-1425/boletingeo.45.2019.484
993 Nockolds, S.R., 1954. Average chemical compositions of some igneous rocks. Bulletin of the
994 Geological Society of America 65, 1007–1032.
995 Paquette, J., Piro, J., Devidal, J., Bosse, V., Didier, A., Sanac, S., Abdelnour, Y., 2014.
996 Sensitivity enhancement in LA-ICP-MS by N2 addition to carrier gas: Application to
997 radiometric dating of U-Th-bearing minerals. Agil. ICP-MS J. 58, 1–5.
998 Parra, M., Mora, A., Sobel, E.R., Strecker, M.R., González, R., 2009. Episodic orogenic front
999 migration in the northern Andes: Constraints from low-temperature thermochronology in
1000 the Eastern Cordillera, Colombia. Tectonics 28. https://doi.org/10.1029/2008TC002423
1001 Paton, C., Woodhead, J.D., Hellstrom, J.C., Hergt, J.M., Greig, A., Maas, R., 2011. Improved
1002 laser ablation U-Pb zircon geochronology through robust downhole fractionation
1003 correction. Geochemistry, Geophys. Geosystems 11.
1004 https://doi.org/10.1029/2009GC002618
1005 Pearce, J.A., Norry, M.J., 1979. Petrogenetic implications of Ti, Zr, Y, and Nb variations in
1006 volcanic rocks. Contrib. to Mineral. Petrol. 69, 33–47.
1007 https://doi.org/10.1007/BF00375192
1008 Pearce, T.H., Gorman, B.E., Birkett, T.C., 1977. The relationship between major element
1009 chemistry and tectonic environment of basic and intermediate volcanic rocks. Earth
1010 Planet. Sci. Lett. 36, 121–132. https://doi.org/https://doi.org/10.1016/0012-
1011 821X(77)90193-5
1012 Pearce, T.H., Gorman, B.E., Birkett, T.C., 1975. The TiO2–K2O–P2O5 diagram: A method of
1013 discriminating between oceanic and non-oceanic basalts. Earth Planet. Sci. Lett. 24,
1014 419–426. https://doi.org/https://doi.org/10.1016/0012-821X(75)90149-1
1015 Perkins, D., 2014. Mineralogy, 3rd ed. Pearson Educación, Harlow.

1016 Pinheiro, S.S., Fernández, P.E.C.A., Pereira, E.., Vasconcelos, E.., Pinto, A.., Montalvão,
1017 R.M.., Issler, R.., Dall'Agnol, R., Teixeira, W., Fernández, C.A.C., 1976. Geología -
1018 Projeto Radar na Amazônia. Folha NA.19-Pico da Neblina, in: Levantamento de
1019 Recursos Naturais- Vol 11. pp. 19–137.
1020 Pinson, W.H., Hurley, P.M., Mencher, E., Fairbairn, H.W., 1962. K-Ar AND Rb-Sr AGES OF
1021 BIOTITES FROM COLOMBIA, SOUTH AMERICA. Geol. Soc. Am. Bull. 73, 907–910.
1022 https://doi.org/10.1130/0016-7606(1962)73[907:KARAOB]2.0.CO;2
1023 Pochon, A., Poujol, M., Gloaguen, E., Branquet, Y., Cagnard, F., Gumiaux, C., Gapais, D.,
1024 2016. U-Pb LA-ICP-MS dating of apatite in mafic rocks: Evidence for a major magmatic
1025 event at the Devonian-Carboniferous boundary in the Armorican Massif (France). Am.
1026 Mineral. 101, 2430–2442. https://doi.org/10.2138/am-2016-5736
1027 Priem, H.N.A., Andriessen, P.A.M., Boelrijk, N.A.I.M., Boorder, H. de, Hebeda, E.H., Huguett,
1028 A., Verdurmen, E.A.T., Verschure, R.H., 1982. Geochronology of the Precambrian in the
1029 Amazonas Region of Southeastern Colombia (Western Guiana Shield). Geol. en Mijnb.
1030 61, 229–242.
1031 PRORADAM, 1979. La Amazonia Colombiana y sus recursos, in: Proyecto Radargramétrico
1032 Del Amazonas. Bogotá, p. 590.
1033 Putzer, H., 1984. The geological evolution of the Amazon basin and its mineral resources.
1034 Springer, Dordrecht, pp. 15–46. https://doi.org/10.1007/978-94-009-6542-3_2
1035 Rahn, M., Seward, D., 2000. How many tracks do we need? Newsl. Int. Fission-Track
1036 Commun 10, 12–15.
1037 Ranst, G. Van, Pedrosa-Soares, A.C., Novo, T., Vermeesch, P., Grave, J. De, 2019. New
1038 insights from low-temperature thermochronology into the tectonic and geomorphologic
1039 evolution of the south-eastern Brazilian highlands and passive margin. Geosci. Front.
1040 https://doi.org/https://doi.org/10.1016/j.gsf.2019.05.011

1041 Restrepo-Pace, P.A., 1995. Late Precambrian to Early Mesozoic tectonic evolution of the
1042 Colombian Andes, based on new geochronological, geochemical and isotopic data.
1043 Ph.D. Dissertation, University of Arizona, Tucson.
1044 Restrepo-Pace, P.A., Cediel, F., 2010. Northern South America basement tectonics and
1045 implications for paleocontinental reconstructions of the Americas. J. South Am. Earth
1046 Sci. 29, 764–771. https://doi.org/10.1016/j.jsames.2010.06.002
1047 Rivers, T., 1997. Lithotectonic elements of the Grenville Province. Review and tectonic
1048 implications. Precambrian Res. 86, 117–154.
1049 Rodriguez, G., Sepulveda, J., Ramirez, C., Ortiz, F., Ramos, K., Bermúdez, J., Sierra, M.,
1050 2011. Unidades , Petrografía y composición quimica del Complejo migmatítico de Mitú.
1051 Boletín Geol. 33, 27–42.
1052 Rollinson, H.R., 1993. Using Geochemical Data: Evaluation, Presentation, Interpretation.
1053 Longman.
1054 Rossoni, M.B., Bastos Neto, A.C., Souza, V.S., Marques, J.C., Dantas, E., Botelho, N.F.,
1055 Giovannini, A.L., Pereira, V.P., 2017. U-Pb zircon geochronologycal investigation on the
1056 Morro dos Seis Lagos Carbonatite Complex and associated Nb deposit (Amazonas,
1057 Brazil). J. South Am. Earth Sci. 80, 1–17. https://doi.org/10.1016/j.jsames.2017.09.021
1058 Santos, J., Rizzotto, G., Potter, P.E., McNaughton, N.J., Matos, R.S., Hartmann, L.A.,
1059 Chemale Junior, F., Quadros, M.E.S., 2008. Age and autochthonous evolution of the
1060 Sunsás Orogen in West Amazon Craton based on mapping and U–Pb geochronology.
1061 Precambrian Res. 165, 120–152.
1062 Santos, J.O.S., Potter, P.E., Reis, N.J., Hartmann, L.A., Fletcher, I.R., McNaughton, N.J.,
1063 2003. Age, source, and regional stratigraphy of the Roraima Supergroup and Roraima-
1064 like outliers in northern South America based on U-Pb geochronology. Geol. Soc. Am.
1065 Bull. 115, 331–348. https://doi.org/10.1130/0016-

7606(2003)115<0331:ASARSO>2.0.CO;2

Santos, J.O.S., Hartmann, L.A., Gaudette, H.E., Groves, D.I., Mcnaughton, N.J., Fletcher, I.R., 2000. A New Understanding of the Provinces of the Amazon Craton Based on Integration of Field Mapping and U-Pb and Sm-Nd Geochronology. Gondwana Res. 3, 453–488. https://doi.org/10.1016/S1342-937X(05)70755-3

Schoene, B., Bowring, S.A., 2006. U–Pb systematics of the McClure Mountain syenite: thermochronological constraints on the age of the 40Ar/39Ar standard MMhb. Contrib. to Mineral. Petrol. 151, 615. https://doi.org/10.1007/s00410-006-0077-4

Stacey, J.S., Kramers, J.D., 1975. Approximation of Terrestrial Lead Isotope Evolution by a 2-Stage Model. Earth Planet. Sci. Lett. 26, 207–221.

Tassinari, C.C.G., 1996. O mapa Geocronológico do Craton Amazônico no Brasil: Revisões dos Dados Isotópicos 257.

Tassinari, C.C.G., Cordani, U.G., Nutman, A.P., Van Schmus, W.R., Bettencourt, J.S., Taylor, P.N., 1996. Geochronological Systematics on Basement Rocks from the Río Negro-Juruena Province (Amazonian Craton) and Tectonic Implications. Int. Geol. Rev. 38, 161–175. https://doi.org/10.1080/00206819709465329

Tassinari, C.C.G., Macambira, M.J.B., 1999. Geochronological provinces of the Amazonian Craton. Episodes 22, 174–182. https://doi.org/10.1080/00206819709465329

Tassinari, C.G., Macambira, J.B., 2004. Geological provinces of the Amazonían Craton, in: Geología Do Continente Sul-Americano: Evolução Da Obra de Fernando Flávio Marques de Almeida. pp. 471–486.

Teixeira, W., Geraldes, M.C., Matos, R., Ruiz, A.S., Saes, G., Vargas-Mattos, G., 2010. A review of the tectonic evolution of the Sunsás belt, SW Amazonian Craton. J. South Am. Earth Sci. 29, 47–60. https://doi.org/10.1016/j.jsames.2009.09.007

Teixeira, W., Tassinari, C.C.G., Cordani, U.G., Kawashita, K., 1989. A review of the

geochronology of the Amazonían Craton: Tectonic implications. Precambrian Res. 42, 213–227. https://doi.org/10.1016/0301-9268(89)90012-0

Teixeira, W., Tassinari, C.C.G., 1976. Geocronologia e consideracoes preliminares sobre a evolugao geológica da Folha NA.21 Pico da Neblina, in: Projeto RADAMBRASIL. Relatório Interno RADAMBRASIL, 67-G, Belém, p. 12.

Thomson, S., E. Gehrels, G., Ruiz, J., Buchwaldt, R., 2012. Routine low-damage apatite U-Pb dating using laser ablation–multicollector–ICPMS. Geochemistry, Geophys. Geosystems 13. https://doi:10.1029/2011GC003928

Veras, R.S., 2012. Petrologia de granitóides dos arredores da Missão Tunuí, NW do Amazonas, Província Rio Negro, Cráton Amazônico. Dissertação. Departamento de Geociencias, Universidade Federal do Amazonas, Manaus.

Vermeesch, P., 2018. IsoplotR: a free and open toolbox for geochronology.

Vesga, C. Castillo, L., 1972. Reconocimiento geológico y Geoquímica preliminar del Río Guaviare, entre la confluencia con los ríos Ariari e Iteviare. Bogotá.

Villagómez, D., Spikings, R., 2013. Thermochronology and tectonics of the Central and Western Cordilleras of Colombia: Early Cretaceous–Tertiary evolution of the Northern Andes. Lithos 160–161, 228–249. https://doi.org/https://doi.org/10.1016/j.lithos.2012.12.008

Wagner, G.A., Van den Haute, P., 1992. Fission-Track Dating. Ferdinand Enke Verlag, Stuttgart. https://doi.org/10.1007/978-94-011-2478-2

Wedepohl, K., 1995. The composition of the continental crust. Geochim. Cosmochim. Acta 59, 1217–1232. https://doi.org/10.1016/0016-7037(95)00038-2

1116 **Table 3** Operating conditions of the LA-ICP-MS equipment

Laboratory & Sample Preparation	
Laboratory name	Géosciences Rennes, UMR CNRS 6118, Rennes, France
Sample type/mineral	Magmatic apatite
Sample preparation	Conventional mineral separation, 1 inch resin mount, 1μm polish to finish
Imaging	CL: RELION CL instrument, Olympus Microscope BX51WI, Leica Color Camera DFC 420C
Laser ablation system	
Mark, Model & type	ESI NWR193UC, Excimer
Ablation cell	ESI NWR TwoVol2
Laser wavelength	193 nm
Pulse width	< 5 ns
Fluence	6.5 J/cm-2 sample AF-4, 6.5 J/cm-2 sample AF-7
Repetition rate	5 Hz sample AF-4, 7 Hz sample AF-7
Spot size	50 µm sample AF-4, 30 µm sample AF-7
Sampling mode / pattern	Single spot
Carrier gas	100% He, Ar make-up gas and N2 (3 ml/mn) combined using in-house smoothing device
Background collection	20 seconds
Ablation duration	60 seconds
Wash-out delay	15 seconds
Cell carrier gas flow (He)	0.75 l/min
ICP-MS Instrument	
Mark, Model & type	Agilent 7700x, Q-ICP-MS
Sample introduction	Via conventional tubing
RF power	1350W
Sampler, skimmer cones	Ni
Extraction lenses	X type
Make-up gas flow (Ar)	0.87 l/min
Detection system	Single collector secondary electron multiplier
Data acquisition protocol	Time-resolved analysis
Scanning mode	Peak hopping, one point per peak
Detector mode	Pulse counting, dead time correction applied, and analog mode when signal intensity > ~ 10_6 cps
Masses measured	$_{43}Ca$, $_{204}(Hg + Pb)$, $_{206}Pb$, $_{207}Pb$, $_{208}Pb$, $_{232}Th$, $_{238}U$
Integration time per peak	10-30 ms

Sensitivity / Efficiency	28000 cps/ppm Pb (50µm, 10Hz)
Dwell time per isotope	5-70 ms depending on the masses
Data Processing	
Gas blank	20 seconds on-peak
Calibration strategy	Madagascar apatite used as primary reference material, Durango and McClure apatites used as secondary reference material (quality control)
Reference Material info	Madagascar (Thomson et al., 2012) Durango (McDowell et al., 2005) McClure (Schoene and Bowring, 2006)
Data processing package used	Iolite (Paton et al., 2010), VizualAge_UcomPbine (Chew et al., 2014)
Quality control / Validation	Durango: Wtd ave ^{207}Pb corrected age = 32.29 ± 0.76 Ma (N=5, MSWD=0.76; probability=0.92) McClure: Wtd ave ^{207}Pb corrected age = 520.3 ± 8.8 Ma (N=3, MSWD=0.47; probability = 0.78)

Table 4 U-Pb LA-ICP-MS data of apatite crystals from Caño Viejita gabbro samples AF-1 and AF-7.

ANALYSIS #	^{238}U/^{206}Pb	PropErr 2Sig%	^{207}Pb/^{206}Pb	PropErr 2Sig%	Approx_U_PPM	Approx_Pb_PPM	Final ^{207}Age	PropErr2SigAbs.
AF-1.1	3.178	5.7	0.4660	2.4	1.4	1.2	997	50
AF-1.2	3.617	5.8	0.4180	2.6	1.3	1.0	973	58
AF-1.3	3.890	3.1	0.3872	2.2	1.7	1.2	960	47
AF-1.4	3.601	3.0	0.4199	2.3	1.2	0.9	974	56
AF-1.5	3.778	2.9	0.4041	2.1	1.2	0.9	959	51
AF-1.6	3.769	3.0	0.3952	1.9	1.5	1.1	973	45
AF-1.7	3.754	3.0	0.4060	2.5	1.1	0.9	965	55
AF-1.8	3.113	3.1	0.4920	2.4	1.2	1.2	960	66
AF-1.9	3.736	3.0	0.4062	2.2	1.2	0.9	966	53
AF-1.10	3.729	3.0	0.4190	2.4	1.1	0.8	943	56
AF-1.11	3.730	3.0	0.3990	2.5	1.1	0.8	980	54
AF-1.12	3.575	3.1	0.4250	2.6	1.2	0.9	971	57
AF-1.13	3.428	3.0	0.4378	2.3	1.3	1.1	985	56
AF-1.14	3.840	3.0	0.3823	2.3	1.4	1.0	977	50
AF-1.15	3.792	2.8	0.3883	1.8	1.7	1.2	976	46
AF-1.16	3.733	2.9	0.3884	2.3	1.5	1.1	999	52
AF-1.17	3.617	2.9	0.4050	2.5	1.2	0.9	997	58
AF-1.18	3.818	2.9	0.3816	2.2	1.6	1.1	989	52

AF-1.19	3.586	2.9	0.4148	2.1	1.2	0.9	984	52
AF-1.20	3.658	3.0	0.4074	2.3	1.4	1.0	983	50
AF-1.21	3.744	3.0	0.3883	2.2	1.3	0.9	997	51
AF-1.22	3.552	3.0	0.4045	2.2	1.3	1.0	1015	56
AF-1.23	3.689	2.9	0.3965	2.1	1.4	1.0	989	52
AF-1.24	3.675	3.0	0.4030	2.7	1.1	0.8	985	57
AF-1.25	3.685	3.0	0.4140	2.4	1.1	0.8	962	60
AF-7.1	3.906	6.2	0.4010	9.2	2.3	1.3	950	120
AF-7.2	3.610	7.2	0.4320	11.6	1.4	0.9	980	140
AF-7.3	3.623	8.0	0.4120	10.9	1.3	0.9	1020	160
AF-7.4	3.268	8.8	0.4210	10.7	1.2	0.8	1090	170
AF-7.5	3.636	6.9	0.3920	10.5	1.6	0.9	1040	130
AF-7.6	3.195	7.7	0.4310	9.7	1.2	0.9	1100	160
AF-7.7	3.484	7.7	0.5170	10.6	1.7	1.3	880	140
AF-7.8	3.300	7.3	0.4220	10.7	1.3	0.8	1110	150
AF-7.9	3.300	8.3	0.4180	10.3	1.1	0.7	1080	150
AF-7.10	3.759	8.6	0.3890	12.1	1.2	0.8	990	150
AF-7.11	3.597	7.6	0.4070	10.1	1.6	1.0	1040	140
AF-7.12	3.322	7.6	0.4250	10.6	1.2	0.9	1080	160
AF-7.13	3.559	7.5	0.4030	10.2	1.2	0.9	1060	140
AF-7.14	3.521	6.3	0.3900	7.7	1.9	1.2	1063	120
AF-7.15	3.759	6.4	0.3670	7.6	2.3	1.5	1062	110
AF-7.16	2.591	7.5	0.5240	8.6	1.4	1.3	1130	190
AF-7.17	2.695	8.1	0.5530	10.1	0.9	0.8	1000	230
AF-7.18	3.096	8.0	0.4690	11.3	1.5	1.0	1070	170
AF-7.19	3.534	10.6	0.5050	14.3	1.0	0.5	900	190
AF-7.20	2.028	7.5	0.5740	7.3	1.6	1.9	1120	190
AF-7.21	1.570	7.1	0.6790	6.2	1.4	2.4	990	230
AF-7.22	3.521	8.5	0.4560	12.1	1.3	0.8	1000	170
AF-7.23	3.436	8.9	0.4360	12.6	1.1	0.6	990	170
AF-7.24	3.125	6.6	0.4590	9.2	1.9	1.4	1080	150
AF-7.25	3.436	8.9	0.4860	13.0	1.0	0.7	1000	190
AF-7.26	3.367	8.4	0.3950	10.9	1.1	0.7	1130	180
AF-7.27	3.690	7.4	0.3930	9.9	1.8	1.0	1020	140
AF-7.28	3.650	8.4	0.4150	12.3	1.3	0.7	1010	150
AF-7.29	3.279	7.9	0.4150	11.6	1.4	0.8	1110	170
AF-7.30	3.636	8.0	0.4720	12.5	1.4	0.8	910	160

AF-7.31	3.472	8.3	0.4350	11.3	1.1	0.6	970	170
AF-7.32	3.279	7.2	0.4270	11.9	1.3	0.7	1110	170
AF-7.33	3.247	8.8	0.4070	10.6	1.1	0.6	1130	160
AF-7.34	3.205	7.4	0.4460	11.7	1.2	0.9	1080	180
AF-7.35	3.378	7.8	0.4740	9.7	1.1	0.9	960	160

1120

Table 5 Apatite fission tracks results. N is the number of analyzed grains, N_s represents the number of spontaneous tracks counted in total, A represents the total area in which N_s were measured distributed over all 33 grains. The Average and Average Weighted $^{238}U/^{43}Ca$ ratios are based on each individual $^{238}U/^{43}Ca$ ratio and are used as a proxy for the Uranium concentration of each apatite grain. The samples pass the chi-squared probability test (>0.05). Chlorine content given in weight percentage and with synthetic apatite (**6.81 wt% Cl,** Klemme et al., 2013). The mean length (l_m), number of tracks lengths (n_l) and standard deviation is also displayed.

Sample	N	N_s	A (10^{-3} cm^2)		Average $^{238}U/^{43}Ca$	Average Weighted $^{238}U/^{43}Ca$	Central age ± 1σ (Ma)	Pooled age ±1σ (Ma)	$P(\chi^2)$	Chlorine content ±1σ (w%)	l_m (µm)	n_l	σ (µm)
AF-7	33	404	3.35		0.0888	0.00934	179.8±9.0	173.3±9.2	0.58	0.28±0.13	11.84	47	1.87